

Searching for Low-Energy Antihelium with the AMS-02 Experiment

A THESIS SUBMITTED TO THE GRADUATE DIVISION OF THE  
UNIVERSITY OF HAWAII AT MĀNOA IN PARTIAL FULFILLMENT OF THE  
REQUIREMENTS FOR THE DEGREE OF

MASTER OF SCIENCE

IN

PHYSICS

December 2022

By

Jesus D. Negrete

Thesis Committee:

Philip von Doetinchem, Chairperson

Veronica Bindi

Jelena Maricic

Keywords: Antihelium, AMS-02, Astrophysics, Cosmic ray

# Acknowledgements

I would like to thank Philip von Doetinchem, my advisor, for allowing me to join his group and for his continued support of this antihelium study. I would like to thank Diego Gómez for helping me throughout the entire process and all the other members of Philip's group for their support.

I would like to gratefully acknowledge the support from the National Science Foundation award #2013228. The technical support and advanced computing resources from University of Hawaii Information Technology Services – Cyberinfrastructure, funded in part by the National Science Foundation MRI award #1920304, are gratefully acknowledged.

Finally, I would like to thank my family and friends for motivating and supporting me throughout my studies.

# Abstract

The search for antihelium nuclei in cosmic rays provides a new opportunity to learn about important problems in modern physics: antimatter asymmetry and the nature of dark matter. Measurements of cosmic rays are being done by the AMS-02 experiment since its installation on the International Space Station. A first-time discovery of cosmic antihelium would be a strong indicator of unknown antimatter sources in our Galaxy. This thesis studies the low-energy region where antihelium has the advantage of having a highly suppressed astrophysical background. This work discusses the techniques utilized for identifying low-energy antihelium and demonstrates how any potential source of background will be adequately suppressed. An antihelium exclusion limit for this low-energy antihelium analysis is set with the results obtained.

# Table of Contents

Acknowledgements . . . . .	ii
Abstract . . . . .	iii
List of Tables . . . . .	v
List of Figures . . . . .	vi
1 Introduction . . . . .	1
2 Astroparticle Physics and AMS-02 . . . . .	3
2.1 Cosmic Rays . . . . .	3
2.1.1 Antimatter in CRs . . . . .	5
2.1.2 Antimatter Asymmetry . . . . .	5
2.1.3 Dark Matter Motivation . . . . .	6
2.2 The AMS-02 experiment . . . . .	8
2.2.1 Transition Radiation Detector (TRD) . . . . .	9
2.2.2 Time Of Flight (TOF) . . . . .	10
2.2.3 Permanent Magnet . . . . .	13
2.2.4 Silicon Tracker . . . . .	13
2.2.5 Anti Coincidence Counter (ACC) . . . . .	15
2.2.6 Ring Imaging CHerenkov (RICH) . . . . .	16
2.2.7 Electromagnetic CALorimeter (ECAL) . . . . .	18

3	Low-energy Antihelium Analysis . . . . .	19
3.1	Standard cut method . . . . .	21
3.1.1	Monte-Carlo analysis . . . . .	24
3.1.2	Data analysis and Exclusion limit . . . . .	28
3.2	BDT Method . . . . .	33
3.2.1	BDT training with data . . . . .	34
3.2.2	MC with BDT . . . . .	36
3.2.3	Data with BDT . . . . .	37
4	Geomagnetic Cutoff Rigidity . . . . .	42
4.1	PLANETOCOSMICS . . . . .	43
4.2	Cutoff Analysis . . . . .	45
5	Conclusion . . . . .	50
5.1	AMS-02 Antihelium Exclusion limit . . . . .	50
5.2	Cutoff Rigidity . . . . .	52
	References . . . . .	53

## List of Tables

3.1	Standard method selection criteria for low-energy antihelium analysis. . . .	22
3.2	Initial cuts, from standard methods selection criteria, applied to data used to train BDT. . . . .	34
4.1	Direction and position binning that is used for the cutoff rigidity analysis. .	45

# List of Figures

2.1	Abundance of elements in cosmic-rays compared to elements in solar-system. Figure from Reference [20]. . . . .	4
2.2	Predicted antihelium flux from different Dark Matter models [47-50,68] and the predicted background [51]. . . . .	7
2.3	View of the AMS-02 experiment with the sub-detectors labeled. . . . .	8
2.4	View of the entire TRD sub-detector. . . . .	10
2.5	The upper and lower TOF planes that make the TOF system. . . . .	11
2.6	View of AMS-02 cylindrical permanent magnet. . . . .	13
2.7	View of one of the silicon tracker layers. . . . .	14
2.8	The assembled inner tracker being set inside the magnet. . . . .	15
2.9	Image of the assembled ACC. . . . .	16
2.10	View of the detection plane and the mirror in the RICH. . . . .	17
3.1	<b>Left:</b> Acceptance distribution of antihelium MC after applying cut groups in selection criteria. <b>Right:</b> Reconstructed mass distribution of antihelium MC multiplied by the particle charge sign. . . . .	24

3.2	<b>Left:</b> Reconstructed mass distribution of antiproton MC multiplied by the particle charge sign. No events remain in the negative mass region. <b>Right:</b> Reconstructed mass distribution from proton MC multiplied by the particle charge sign. No events remain in the negative mass region. . . . .	25
3.3	Reconstructed mass distribution from helium MC multiplied by the particle charge sign. . . . .	26
3.4	Reconstructed mass distribution for data using the selection criteria from the Standard method. . . . .	28
3.5	<b>Left:</b> Interpolated acceptance distribution from antihelium after entire selection. <b>Right:</b> Exposure time utilizing the IGRF geomagnetic cutoff calculation. . . . .	30
3.6	The number of events per rigidity bin from data and the helium-4 MC to demonstrate the size of the MC will properly account for the events in data.	31
3.7	The exclusion limit obtained with Standard method for 10 years. Predicted antihelium flux from different Dark Matter models [47-50, 68] and the predicted background [51]. . . . .	32
3.8	Signal (blue) and background (red) efficiency as a function of the BDT value.	36
3.9	<b>Left:</b> Reconstructed mass distribution for antihelium MC with the BDT method. <b>Right:</b> Antihelium MC acceptance that has comparison between BDT and Standard method. BDT includes the cut on mass like in Fig. 3.1. . . . .	37
3.10	<b>Left:</b> Reconstructed mass distribution for antiproton MC with the BDT method. <b>Right:</b> Reconstructed mass distribution for proton MC with the BDT method. . . . .	38
3.11	Helium MC reconstructed mass distribution with the BDT method. . . . .	38
3.12	Reconstructed mass distribution for data with the BDT method. . . . .	39

3.13	Event display of one event in data that remains after BDT cut. Event has a bad $\chi^2 Y$ value with the Choutko algorithm. . . . .	40
3.14	Event display of second event in data that remains after BDT cut. Event had two particle tracks measured. . . . .	40
3.15	Event display of third event in data that remains after BDT cut. Event had two hits on the ACC. . . . .	41
4.1	Visual by PLANETOCOSMICS of tracks being back traced at a position for a direction at different rigidity values. . . . .	44
4.2	<b>Left:</b> Trajectory of a particle reaching the starting position from a direction that is below the local horizon. <b>Right:</b> Example of how a circular cone at a position in the magnetosphere would look for a rigidity $R$ (right cone is forbidden cone). Images from Ref. [78] . . . . .	46
4.3	Forbidden probability histogram for a position (altitude [km], latitude [deg], longitude [deg]) and direction (zenith [deg], azimuth [deg]). . . . .	47
4.4	Forbidden probability plot used to get more accurate cutoff rigidity value. Dashed lines show the effective cutoff rigidity obtained by original method. . . . .	48
4.5	<b>Left:</b> Cutoff rigidity, with 100% allowed tracks, histogram created by looking at all directions for a position. <b>Right:</b> Cutoff rigidity map for May 19, 2011, for 100% allowed tracks. The black dashed lines demonstrate a $ Latitude  < 51.6^\circ$ which the ISS travels. . . . .	49

# Chapter 1

## Introduction

An important open question in modern physics is the asymmetry in the density between antimatter and matter in the Universe. There is no clear explanation for this difference, but one solution comes from the existence of antimatter objects in the Universe that has yet to be detected directly [1]. Another issue in physics is the mysterious nature surrounding Dark Matter. Dark Matter comprises most of the gravitational matter in the Universe and is non-luminous. Studying these problems in physics would bring a better understanding of the origin of the Universe and its evolution.

Cosmic Rays (CRs) are atomic nuclei that are products of energetic astrophysical processes in our Galaxy, like supernovae explosions and supernova remnants [2]. CR antimatter is mostly comprised of positrons, created in pulsars, and antiprotons, created from primary CRs interacting with the interstellar medium (known as secondary production). AMS-02 has already detected antimatter in CRs like positrons, and antiprotons [3-14] (and potentially antihelium [15]). Many Dark Matter (DM) models state that the annihilation or decay of these candidate particles could create Standard Model (SM) particles [16]. This means the signal from Dark Matter annihilation's should contaminate the flux of CR particles. The low flux of antiparticles allows the signal-to-background from Dark Matter annihilation's to be better. Antihelium is a heavier antiparticle that possesses

a challenge in detection, due to its low production compared to lighter antiparticles. Any detection at low energies would be signaling to sources beyond the standard model. Winkler [50,68] discusses an aspect overlooked that could explain the potential antihelium candidates at higher energies.

The Alpha Magnetic Spectrometer (AMS-02) experiment is a multi-purpose CR detector mounted on the International Space Station (ISS) since 2011. The objective of the experiment is to measure the flux of CRs and antinuclei in CRs over a wide energy range in space.

The thesis will discuss the following in the next chapters. Chapter 2 provides the background information on astroparticle physics and CRs. A description of the AMS-02 experiment and its sub-detectors are also discussed. Chapter 3 details the methodology for the low-energy antihelium analysis with Monte Carlo simulations and analysis of the AMS-02 data from 2011 to 2021. Details on the background suppression from potential sources and on the estimation of the antihelium exclusion limit determined are shown in this chapter. Chapter 4 focuses on better understanding the geomagnetic cutoff rigidity at low energies for antinuclei studies. Chapter 5 summarizes the results obtained in this thesis.

# Chapter 2

## Astroparticle Physics and AMS-02

### 2.1 Cosmic Rays

Light from the Sun and more distant stars was the main type of extraterrestrial radiation known until the discovery of cosmic rays was made by Victor Franz Hess in 1912 [17,18]. Cosmic Rays are a unique type of radiation referring to highly energized charged particles that the Earth experiences. Investigations into the nature and origin of CRs are helping to reveal new astrophysical phenomena, and in unraveling the mystery surrounding the nature of dark matter. The CR field is an important cross-disciplinary area of in-depth research that is explored by particle and astrophysics to solar and planetary phenomena.

Cosmic Rays are atomic nuclei that are mainly composed of protons (86%), helium (11%), and other elemental particles like electrons (2%) and neutrinos (less than 1%) [20]. All other elements in the periodic table could potentially be found in CRs because all elements can technically be produced during element formation. Cosmic Ray origin is a problem that is still not completely understood, but some particles are known to be produced and accelerated by astrophysical events in our Galaxy. The astrophysical sources are very energetic like supernova explosions (SNE), supernova remnants (SNRs), pulsars, accretion black holes, and active galactic nuclei (AGN). Primary CRs refer to particles

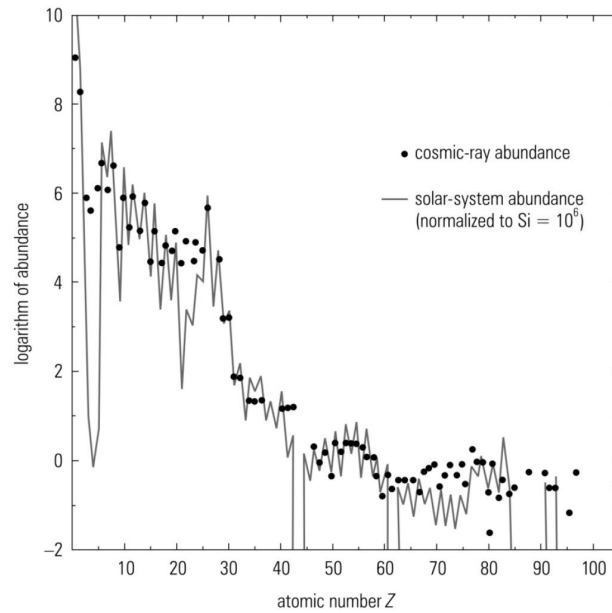


Figure 2.1 Abundance of elements in cosmic-rays compared to elements in solar-system. Figure from Reference [20].

that are essentially unaltered after being produced by an astrophysical source. Secondary CRs are particles that are produced from primaries interacting with the interstellar medium or by the decay of unstable nuclei. Figure 2.1 shows the abundance of elements in CRs in comparison to the elements in the solar system. The abundance shown between CRs and the solar system is comparable in their magnitudes except for some. The difference is apparent in Lithium, Beryllium, and Boron (charge  $Z=3$  to 5). These three light elements are more abundant in CRs because they are secondary CRs that are produced by the fragmentation of heavier nuclei, like Carbon and Oxygen, interacting with the interstellar medium. The fluxes of nuclei from CRs have been measured by experiments like PAMELA and AMS-02 with great precision [22-29].

### 2.1.1 Antimatter in CRs

Antimatter has been detected in CRs and they account for less than 0.01% of particles. The first experimental observation of antimatter was a positron, by Carl David Anderson while studying CR tracks in a cloud chamber in 1932 [30]. Antiprotons would later be observed in the Bevatron accelerator in 1955 [31] and soon after antineutrons. Antideuterons would be the first antinucleus to be observed at the Brookhaven National Laboratory in 1965 [32]. Antiprotons and antideuterons are produced in our Galaxy as secondaries, although antideuterons have not yet been detected in CRs. The first detection of antiprotons in CRs would not occur until the late '70s by Golden *et al.* [4] and Bogomolov *et al.* [5] using spectrometers. Antimatter is produced more commonly now in collider experiments. A large portion of antimatter is in CRs that come from secondary production, but the flux of antiparticles that reach the Earth is reduced. In recent years, experiments like PAMELA [27,28], and AMS-02 [22-26] have moved CR measurements to the precision era. There is still some ambiguity on whether antiprotons are purely of secondary origin or if they may contain hints of originating from exotic sources.

### 2.1.2 Antimatter Asymmetry

Our observable Universe is matter dominated and the disparity in the density between antimatter and matter makes this apparent. This difference in the observable Universe still does not have a clear explanation and hinders the understanding of the evolution of the universe. Antiparticles in CRs provide an intriguing method of learning about the antimatter in our universe. A proposed answer to the discrepancy would come from detecting antimatter regions in our Galaxy. A possible explanation suggests that anti-clouds or anti-stars would be regions in our Galaxy that would be capable of creating antiparticles [1]. This assumption is challenging because this type of source has not been

detected before. Antiparticle detection is rare since they account for less than 0.01% of CRs and cosmic antihelium in a low-energy region pose an enormous challenge with a unique advantage. Antihelium is not produced as commonly as lighter, more abundant cosmic antiparticles like positrons and antiprotons. Any detection of antihelium in CRs would be an indicator of processes that could not be explained by standard methods. Thus, low-energy antihelium in CRs are an excellent candidate for detecting antimatter objects in our Galaxy that could emit antiparticles [2].

### **2.1.3 Dark Matter Motivation**

Observations have shown that the observable Universe accounts for less than 5% of its mass density. The Universe is comprised of Dark Matter (27%) and Dark Energy (68%) which are non-luminous. This means that DM is roughly five times more abundant than standard model matter and its nature remains a mystery [33-35]. Dark matter has been confirmed to exist through observations of Galaxy rotations, Cosmic Microwave Background anisotropy, gravitational lensing, and the movement of Galaxy clusters [36-44]. Understanding the nature of DM would be important in understanding our Universe and its evolution. A potential method of learning more about DM is through indirect detection.

Some models theorize that SM particles can be created through the annihilation or decay of DM because DM was in thermal equilibrium with SM particles in the early Universe [17]. The resulting particles would contribute to the regular CR flux and hence provide a gateway to revealing the nature of DM. Final state DM-induced particles are expected to be at low energies because of the low-velocity DM distribution near Earth. Although this excess should be present in any type of cosmic radiation, the abundance of matter from astrophysical sources limits its detection. The DM excess can have a better signal-to-background in antiparticles because antimatter is less abundant in the

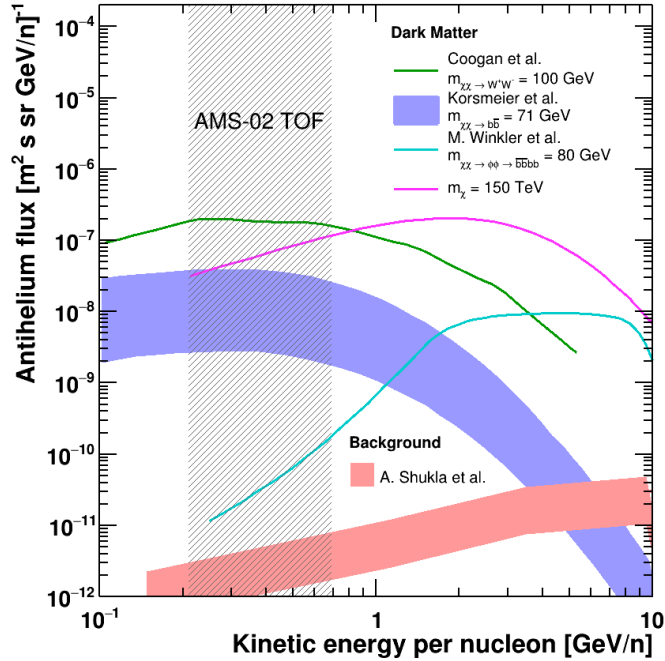


Figure 2.2 Predicted antihelium flux from different Dark Matter models [47-50,68] and the predicted background [51].

Universe than matter. It is in this context where antimatter, and particularly antihelium, becomes a golden candidate to observe DM indirectly. The only possible source of background for antihelium is secondary antihelium produced from CRs interacting with the interstellar medium. However, antihelium has a high energy threshold for production and the steep energy spectrum of CRs means that few particles would have sufficient energy to produce secondary antihelium. Any that would be produced would have a relatively large kinetic energy as shown in Fig. 2.2. Therefore, low-energy cosmic antihelium can be a potential breakthrough approach for indirect DM searches. Some theorize that the excess measurement in the positron fraction around 10GeV needs an additional source like DM to explain, but this anomaly continues to be debated [45,46]. Thus, antihelium at low energies would be an unambiguous signal for an exotic source like DM, that could not be explained by standard models.

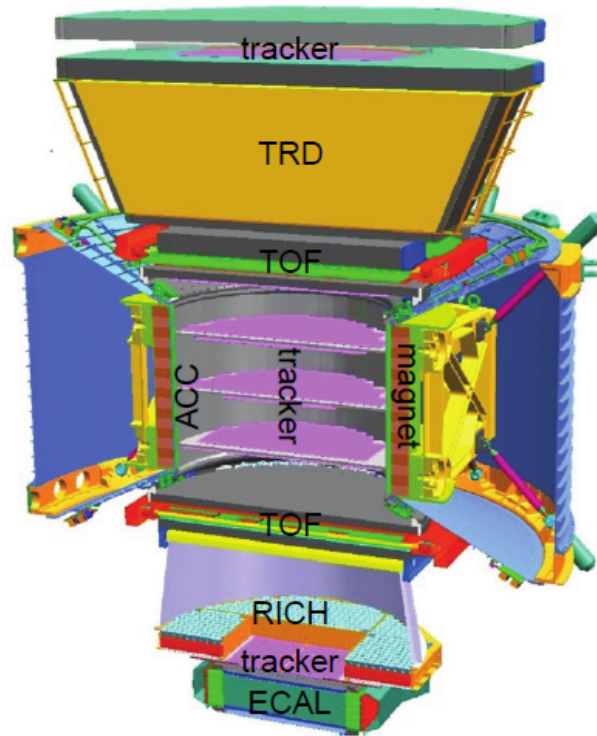


Figure 2.3 View of the AMS-02 experiment with the sub-detectors labeled.

## 2.2 The AMS-02 experiment

The Alpha Magnetic Spectrometer (AMS-02) is a space-based multi-purpose particle detector that has been operating on the ISS since May 2011. The objective of the experiment is to measure the spectrum of CRs from 500MeV/c to a few TeV/c momenta per nucleon. Included in the mission of the experiment are the measurements for antimatter, the origin of cosmic rays, searching for dark matter, and the investigation of new astrophysical phenomena.

The AMS-02 had a successful precursor, AMS-01, that was boarded on the Space Shuttle Orbiter Discovery for ten days in June 1998. The detector produced significant

results by collecting over one hundred million cosmic ray events for roughly 180 hours [52-56].

A schematic overview of the AMS-02 detector is shown in Fig. 2.3. The detector contains a Transition Radiation Detector (TRD), a Time of Flight (TOF) system with four layers, a permanent magnet, a nine-layer silicon tracker, an Anti Coincidence Counter (ACC) array, a Ring Imaging Cherenkov counter (RICH), and a 3D sampling Electromagnetic Calorimeter (ECAL). The AMS-02 uses a Cartesian coordinate system with the origin located at the center of the magnet. The  $X$ -axis is parallel to the magnetic field in AMS-02 while the  $Y$ -axis is perpendicular to the magnetic field. The  $Z$ -axis thus corresponds to the vertical axis of AMS-02, with the positive  $Z$  region pointing towards the TRD and negative  $Z$  pointing towards the ECAL. The  $YZ$  plane is known as the "bending plane" because the magnetic field deflects charged particles to this plane alone.

### **2.2.1 Transition Radiation Detector (TRD)**

The TRD [57], at the top of AMS is used for distinguishing between electrons and protons and can obtain the charge of light nuclei. Transition Radiation is the physical principle of a charged particle emitting electromagnetic radiation when traversing through two media that have different dielectric constants. This radiation is produced in the detector when highly relativistic charged particles pass through the 20mm thick fleece radiator material with a density of  $0.06\text{g/cm}^3$ . The transition radiation photons are detected in proportional mode by straw tube modules filled with a 90:10 Xe:CO<sub>2</sub> mixture. The TRD consists of 20 straw layers that are separated by the 20mm fleece radiators. Modules consist of 16 straw tubes arranged in parallel with an inner diameter of 6mm and lengths up to 2m. There are a total of 328 straw tube modules and 5248 proportional tubes. These layers are arranged in a conical-shaped octagon structure as seen in Fig. 2.4. The top and bottom four layers are

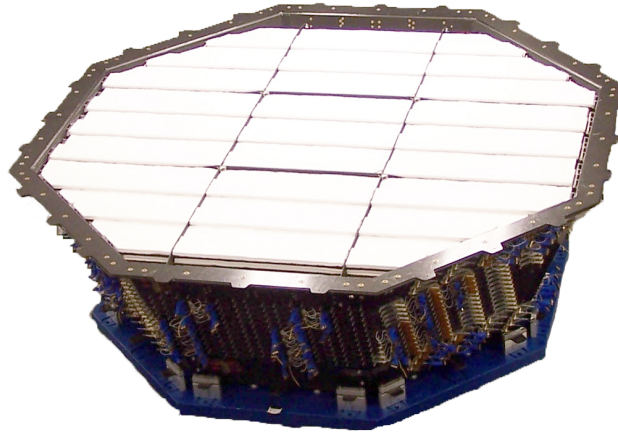


Figure 2.4 View of the entire TRD sub-detector.

arranged parallel to the AMS-02 magnetic field while the inner 12 layers are perpendicular to the magnetic field to provide 3D tracking. The TRD separates electrons from protons by their transition radiation intensity, which is proportional to the particle relativistic Lorentz factor  $\gamma = E/m$ . An analog pulse height readout is used in distinguishing the signal, and electrons and positrons can be selected with 90% efficiency.

### 2.2.2 Time Of Flight (TOF)

The TOF [58-60] system provides the fast trigger signal to the experiment, shown in Fig. 2.5. It measures the velocity  $\beta$  and the absolute charge  $Z$  of charged particles and can distinguish if a particle is going up or down concerning the detector's coordinate system. The detector is formed by four layers that contain 34 plastic scintillator paddles in total, which are read out by fine-mesh Hamamatsu R5946 PhotoMultiplier Tubes (PMTs). Each paddle is made up of EJ-200 polyvinyltoluene plastic scintillators, manufactured by Eljen-Technology, which are 1cm thick. The Upper TOF (UTOF), comprised of layers 1 and 2, is located above the magnet and below the TRD. Layer 1 contains 8 scintillator paddles



Figure 2.5 The upper and lower TOF planes that make the TOF system.

oriented parallel to the magnetic field direction (X-axis) and Layer 2 has 8 scintillator paddles oriented perpendicular to the magnetic field (Y-axis). The Lower TOF (LTOF), comprised of layers 3 and 4, is located below the magnet and above the RICH. Layer 3 contains 10 scintillator paddles oriented perpendicular to the magnetic field and layer 4 has 8 paddles oriented parallel to the magnetic field.

Every layer has the central paddles being rectangular while the edge paddles are trapezoidal to cover the AMS-02 acceptance. A paddle will vary in length between 117 to 134cm. The central paddles have a total of 4 PMTs at their ends, each end having 2. The edge paddles for layers 1 and 4 each have 6 PMTs, and layers 2 and 3 have 8 PMTs each. The TOF has a total of 134 PMTs and the layers being grouped help to avoid geometrical inefficiencies.

A particle crossing the plastic scintillator will deposit energy that can be used to determine the absolute value of the electric charge  $Z$ . The charge is measured by using the

PMT anode signal that comes from both sides of a counter. The resolution from the TOF for charge  $|Z|=2$  particles is measured to be  $\Delta Z=0.06$ . The TOF system reconstructs a particle's velocity  $v$ , where  $v=\beta c$ , from the precise time measurement  $t = l_p/v$  of a particle going from UTOF to the LTOF. The path length is obtained by  $l_p = L/\cos \theta$ , where  $L$  is the distance between the two TOF planes, which is 127.3 cm, and  $\theta$  is the tracks zenith angle. The timing is measured by:

$$t = \frac{L}{c\beta \cos \theta}. \quad (2.1)$$

Each counter has a timing resolution measured to be less than 180 ps and is parameterized by:

$$\sigma = \sqrt{\frac{P_1^2}{Z} + P_2^2}. \quad (2.2)$$

The parameters  $P_1$  and  $P_2$  are equal to  $(159 \pm 2)$ ps and  $(79 \pm 1)$ ps respectively. Assuming that the time measurement has a Gaussian uncertainty, yield's:

$$\frac{\sigma_t^2}{t^2} = L^2 \left( \frac{\sigma_v^2}{v^2} + \frac{\sigma_{\cos\theta}^2}{\cos^2 \theta} \right). \quad (2.3)$$

This can then be simplified by the uncertainty in the zenith measurement being very small. After dropping this term, the resolution for high velocity particles is:

$$\frac{\sigma_v}{c} = \frac{c \cdot \cos \theta}{L^2} \sigma_t. \quad (2.4)$$

The velocity and direction measured for  $|Z|=2$  particles have a resolution of  $\Delta\beta/\beta^2 \approx 2\%$ . The timing resolution of the TOF can check whether a particle is going upward or downward at the  $10^{-9}$  level, and is a fundamental aspect in searching for antimatter.

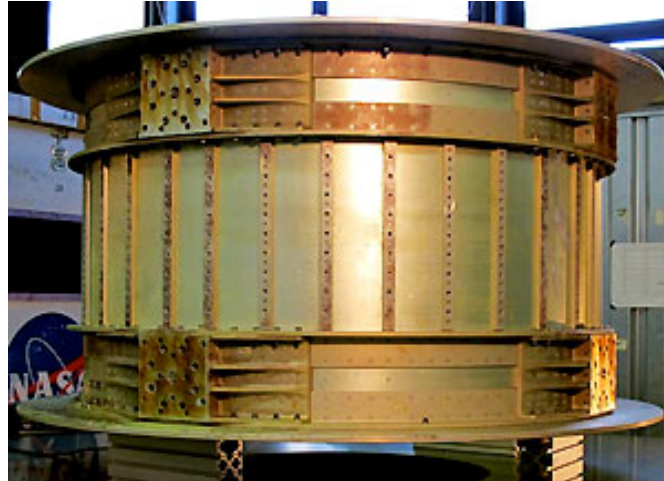


Figure 2.6 View of AMS-02 cylindrical permanent magnet.

### 2.2.3 Permanent Magnet

The permanent magnet [61] is one of the most important pieces of AMS-02 as it bends charged particle tracks with a magnetic field strength  $B = 0.149\text{T}$  to determine their rigidity (momentum per charge). The magnet is recycled from the previous experiment, AMS-01, and is comprised of 64 high-grade Nd-Fe-B sectors placed into a cylindrical structure that has an inner diameter of 110cm and is 80cm long as seen in Fig. 2.6. The magnetic field, about the AMS-02 coordinate system, points along the  $X$ -axis. The magnet is configured in such a way so that the external magnetic field is negligible. The measured field strength 2m from the center of the magnet is measured to be less than 3G so the field outside should not affect the station.

### 2.2.4 Silicon Tracker

The silicon tracker [61,63] measures the electric charge and the rigidity of particles with its 9 layers. The nine layers of the tracker are composed of double-sided silicon micro-strip detectors that are 0.3mm thick as seen in Fig. 2.7. Layer 1 is located above the TRD, layer

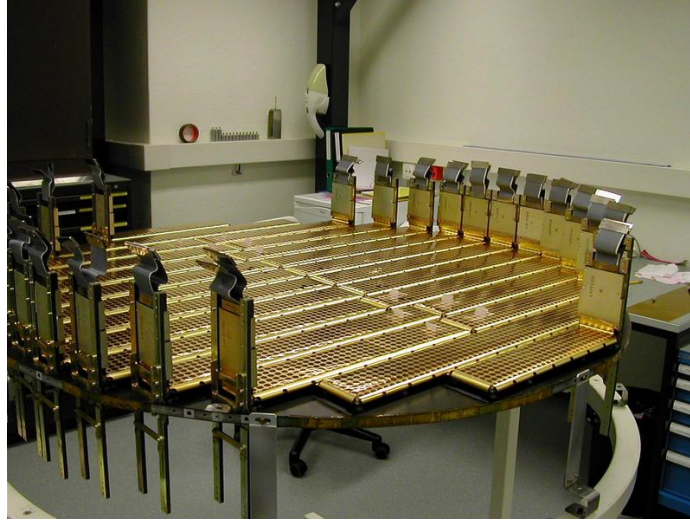


Figure 2.7 View of one of the silicon tracker layers.

2 is above the magnet and below the UTOF, and layer 9 is in between the RICH and the ECAL. These single layers make three planes while layers 3 to 8 are arranged to form a double-sided plane. Layers 3 and 4, 5 and 6, and 7 and 8 come in pairs and make up the inner tracker inside the magnet along with layer 2 being above the magnet. The planes that comprise the inner tracker are mounted onto a cylindrical carbon fiber structure so that they can be set inside the magnet as shown in Fig. 2.8. A particle that passes through one of the silicon trackers will produce a signal through the ionization at the plane. Each tracker plane obtains an independent value of a particle's absolute charge with the deposited ionization energy proportional to the square of the charge ( $I \propto Z^2$ ). The charge resolution from the silicon tracker is  $\Delta Z = 0.06$  for charge two particles.

The ionization provides a signal that is used to estimate the traversing position of a particle on the surface with an accuracy of  $10\mu\text{m}$  in the bending direction (Y) and  $30\mu\text{m}$  in the non-bending direction (X). A laser system of 20 infrared beams monitors the mechanical stability of the inner tracker with a position accuracy of  $5\mu\text{m}$  or better by having a beam that penetrates all layers. The precise measurements of a particle by the



Figure 2.8 The assembled inner tracker being set inside the magnet.

tracker planes, 3 planes inside the magnetic field and one outside, allow for the trajectory of a particle that may bend in the magnet to be well determined. The rigidity of a charged particle traveling through the detector is obtained by:

$$R = \frac{pc}{Z} = B\rho. \quad (2.5)$$

The magnetic field intensity  $B$  and the trajectories radius of curvature  $\rho$  gives an accurate value for the rigidity which has a resolution of 25% at 500 GV [62]. The precise measurements of the silicon tracker are accomplished with its 2284 micro-strip detectors which make 192 ladders that contain the silicon sensors, readout electronics, and mechanical support for the planes.

### 2.2.5 Anti Coincidence Counter (ACC)

The ACC system surrounds the inner tracker, as shown in Fig. 2.9, to ensure particles have a clean track reconstruction [64]. The system is placed in the inner bore of the

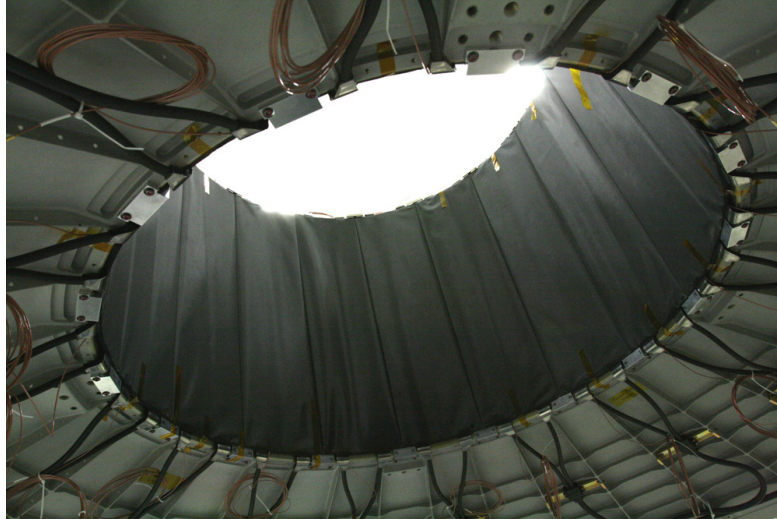


Figure 2.9 Image of the assembled ACC.

magnet with a modular design that consists of 16 plastic curved scintillator panels. Each panel is embedded with wavelength-shifting fibers and they have a dimension of 826mm long, 230mm wide, and 8mm thick. A hit on the ACC could indicate that an event has an unwanted particle coming from the side of the detector. Very high-energy events can have hard interactions occurring in the inner tracker which would produce secondary tracks that would exit through the side and trigger the ACC. The system provides information on secondaries created by cosmic rays interacting with the detector and the backscattering on the ECAL. The ACC gives a veto to a particle that travels through the side at the same time as another particle passing through the inner tracker and TOF system. A veto in these cases ensures the event is a clean sample with a detection efficiency greater than 0.9999.

### **2.2.6 Ring Imaging CHerenkov (RICH)**

The RICH [65] sub-detector, located between the LTOF and the ECAL, is designed to measure a particle's charge and velocity ( $\beta$ ). The top plane consists of two dielectric radiators that are non-overlapping. The central area of the plane has 16 tiles of sodium

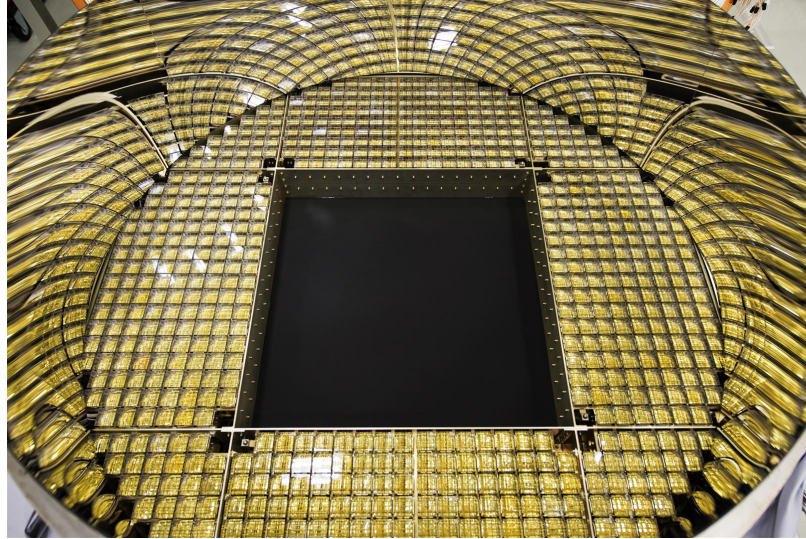


Figure 2.10 View of the detection plane and the mirror in the RICH.

fluoride crystals that are 5mm thick with a refractive index  $n = 1.33$  surrounded by 92 tiles of silica aerogel that are 2.5cm thick with a refractive index  $n = 1.05$ . The bottom plane is composed of 680 4x4 multi-anode PMTs which detect the Cherenkov light emitted by the cosmic rays that interact with the radiator and an empty rectangular area in the center to match the area of the ECAL beneath it. The radiator (top plane) is separated from the detection plane (bottom plane) by 46 cm and has a highly reflective conical mirror in the inner lateral surface between them as shown in Fig. 2.10. The mirror reflects Cherenkov rings that would otherwise not be visible back onto the detection plane to increase the geometrical acceptance. Particles with a velocity that exceeds the threshold velocity of  $1/n$  emit Cherenkov light and these photons have an angle  $\theta$  concerning the direction of the particle. RICH determines a particle's velocity over a wide energy range by measuring the Cherenkov angle with a high resolution of 0.001 on  $\beta$ . The absolute charge of a particle is deduced by the intensity of the Cherenkov light emitted making the light cone and can obtain the charge for nuclei up to iron.

### 2.2.7 Electromagnetic CALorimeter (ECAL)

The ECAL [66] provides precise 3D imaging reconstructions of showers initiated by leptons and photons. The ECAL is located at the very bottom of the AMS-02 detector. The calorimeter consists of 9 superlayers that are 1mm thick lead interleaved with 10 layers of scintillating fibers that are 1mm thick. Leptons and hadrons are separated by the ECAL with a rejection power of  $10^4$  in the energy region from 1GeV to 1TeV with an energy resolution parameterized by:

$$\frac{\sigma(E)}{E} = \frac{(10.4 \pm 0.2)\%}{\sqrt{E/GeV}} \oplus (1.4 \pm 0.05)\% \quad (2.6)$$

# Chapter 3

## Low-energy Antihelium Analysis

Antihelium in cosmic rays is a challenge to detect because of the disproportion of antimatter in the Universe and the scarceness of heavier antinuclei. The lack of cosmic antihelium gives it the unique advantage of also having a strongly suppressed astrophysical background at the low-energy region being explored. This chapter discusses in detail the different methods used to identify antihelium and how these methods suppress the potential background that could appear.

Cosmic antihelium will be identified by looking at the reconstructed mass for events:

$$m = ZR\sqrt{\frac{1}{\beta^2} - 1}. \quad (3.1)$$

$Z$  is the absolute charge of a particle obtained by the Inner Tracker and TOF. The charge is assumed to be an integer when calculating the mass.  $R$  is the rigidity (momentum/charge), and  $\beta$  is the particle velocity measured by the TOF which allows this work to investigate a low-energy region.

### Potential Background

For  $|Z|= 2$ , the expected particles are helium-4 and helium-3. Helium has the same absolute charge as antihelium and is the most abundant CR that can fake antihelium.

The tracker misidentifying the charge sign of helium CRs makes them potential sources of background because they have the same  $|Z|$  as antihelium. A large helium-4 MC sample is investigated to properly understand if and how a helium event can be incorrectly reconstructed as antihelium.

Protons and antiprotons have a  $|Z|=1$  and are the most abundant CRs for matter and antimatter, respectively. Since these  $|Z|=1$  particles are so abundant they could be misreconstructed as antihelium if their charge is measured incorrectly. High-velocity particles can have their charge sign misidentified because their track is not bent significantly by the magnetic field. For low energies the confusion should be negligible. To ensure that these  $|Z|=1$  species are not misreconstructed as antihelium, a large MC sample for antiprotons and protons is looked at.

For this work, two different methods will be discussed, a Standard cut and a Boosted Decision Tree (BDT) method. The variables that are used for the Standard cut method are adopted from the previous work in Ref. [67] for antideuterons. The cut regions are modified to identify low-energy antihelium events. The BDT method selects good antihelium events with quality track variables from the Standard method. The BDT method was incorporated as an alternative way to search for antihelium events. It is incorporated into the Toolkit for Multivariate Analysis (TMVA) which provides parallel processing of the training and testing of events [70]. This would help to improve some of the cuts in the Standard method that may be too restrictive that could be rejecting potential antihelium candidates. This analysis is performed by working with Monte-Carlo simulations to build a framework that is then applied to data to identify low-energy antihelium nuclei.

## **Minimum Cuts**

Before discussing the methods used to search for the particle of interest, both methods have some necessary cuts that must be applied to the data. These minimum cuts are required to check that an event in data has the minimum number of required measurements and that

the measurements were taken during times when the detector is operating normally. There are a series of bad run cuts that are specific for an AMS analysis and these cuts exclude runs that were tagged as bad. Another cut involves excluding flight times that are in the South Atlantic Anomaly (SAA) region. In this region, the geomagnetic field is close to the Earth's surface, and this causes a high trigger rate. The other cuts are for checking that events have AMS exposure time information, a physics trigger measurement, and a particle track measured. The last cut is to verify a particle has entered from the top of the detector's field of view.

### **3.1 Standard cut method**

This section discusses the implementation of a direct cut-based analysis, referred to as the Standard method, to search for cosmic antihelium. The entire list of cuts applied for this method is listed in Table [3.1]. The first group of variables looked at are the preselection cuts. The preselection cut group requires events to have activated the physics trigger and that the velocity ( $\beta$ ) of a particle is in the TOF range. The physics trigger is built by having 4 out of 4 of the TOF planes to form a coincidence signal. The geometrical cut group is important in verifying that a particle is within the detector's volume. The first variable checks the track's zenith angle at layer 2 is in line with a CR entering from the top of the AMS detector. The next variables check a particle's zenith angle and the radial distance obtained 100 cm below the center of AMS-02. The last variable for the geometrical cut group checks that the position of an event at every tracker layer is within 2cm of the layer's length.

#### **Charge cuts**

The particle charge is important in identifying an event as antihelium. The particle charge is obtained by the inner tracker and the TOF. The cut on the charge from the inner

Table 3.1 Standard method selection criteria for low-energy antihelium analysis.

Variable	Cut		Group
Physics trigger	=	1	Preselection cut
Velocity ( $\beta$ )	>	0.5 < 0.85	Preselection cut
Tracker Layer 2 theta		< 45	Geometrical cut
Tracker theta (at Z=-100cm)		< 45	Geometrical cut
Tracker radial distance (at Z=-100cm)		< 80	Geometrical cut
In Tracker Layers	$\geq$	1	Geometrical cut
Inner Tracker Charge	>	1.7 < 2.7	Charge cut
UTOF Charge	>	1.7 < 2.7	Charge cut
LTOF Charge	>	1.7 < 2.7	Charge cut
Inner Pattern	=	1	Inner tracker cut
Inner Tracker XY (Y) Hits	$\geq$	4	Inner tracker cut
Tracker Track Normalized $\chi^2$ X	>	0 < 5	Inner tracker cut
Tracker Track Normalized $\chi^2$ Y	>	0 < 5	Inner tracker cut
$\chi^2$ X Difference (Kalman-Choutko)	>	-5 < 5	Inner tracker cut
$\chi^2$ Y Difference (Kalman-Choutko)	>	-6 < 6	Inner tracker cut
TOF clusters Associated with Particle	=	4	TOF cut
TOF BetaH Spatial Normalized $\chi^2$	$\geq$	0 < 2	TOF cut
TOF BetaH Timing Normalized $\chi^2$	$\geq$	0 < 5	TOF cut
TRD Electron Helium Log Likelihood	$\geq$	0.4	TRD Likelihood cut
ACC Hits		$\leq$ 1	Interaction cut
Number of Tracks	=	1	Interaction cut
Number of Particles	=	1	Interaction cut

tracker, and the upper and lower TOF layer are wide. The lower bound charge limit removes any particles that have a  $|Z|=1$  and allows for any  $|Z|=2$  particles that may have had their charge value determined to be lower than expected. The upper bound value is allowed to be much further away from  $|Z|=2$  because no antiparticles heavier than antihelium can be potential background in this region, but the limit still excludes any  $|Z|=3$  particles.

### Inner tracker cuts

The other selection groups are instrumental in verifying that a candidate event has a good quality track. The first cut in the inner tracker group, the inner pattern, is an important requirement that a particle hit all the inner tracker planes. This is useful in assuring the

particle crossed the entire inner portion. The minimum number of inner tracker  $XY$  and  $Y$  hits associated with the AMS particle is 5. Since the inner tracker measured the charge and rigidity of a particle, enough hits must be obtained to get good values. The normalized  $\chi^2$  is required to be less than 5 for the  $X$  fit, which is the non-bending plane, and the  $Y$  fit, which is the bending plane. A  $\chi^2$  fit compares the observed and expected track for the bending ( $Y$ ) and non-bending ( $X$ ) direction. The  $\chi^2$  value demonstrates the similarity between the tracks and this information is important for knowing the quality of an event passing through the detector. The tracker track fit is used in getting the inverse of the rigidity by determining the radius of curvature of a track. The fitting algorithm for these tracker track fits uses the Kalman method. The last two variables in the inner tracker cut group are to ensure that the  $\chi^2$  for the  $X$  and  $Y$  fit using the Choutko method are near those obtained with Kalman. The Kalman method uses some information from the positions measured to predict where the particle will go next. The Choutko method is a technique that is specific to an AMS-02 analysis.

### **TOF cuts**

To ensure that the TOF reconstructs the best possible velocity value, the cuts in the TOF cut group is important. The number of TOF clusters associated with an AMS particle makes sure that all 4 TOF layers are used for the velocity reconstruction. The normalized  $\chi^2$  spatial fit is set to be less than 2 and  $\chi^2$  of the timing fit must be less than 5. The spatial fit compares the tracker track to the TOF clusters. The timing fit compares the timing of the TOF clusters with the tracker tracks.

### **TRD and Interaction cuts**

The TRD likelihood cut is important in rejecting electrons from antihelium. The TRD is used to suppress light mass mesons by the transition radiation produced from highly relativistic particles. The signal measured by the TRD allows for the separation to occur because it is proportional to the particles energy and mass. Light nuclei may

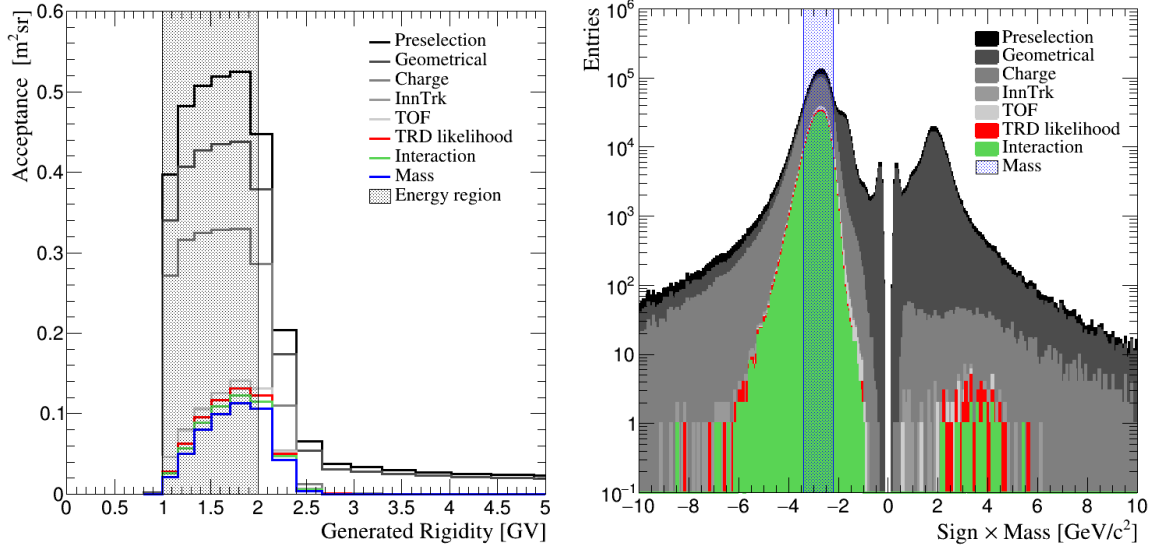


Figure 3.1 **Left:** Acceptance distribution of antihelium MC after applying cut groups in selection criteria. **Right:** Reconstructed mass distribution of antihelium MC multiplied by the particle charge sign.

not contaminate the antihelium signal largely so a loose cut on the electron-helium log likelihood is implemented to suppress background from these events. The number of ACC hits cut in the interaction group is important for excluding events that may have simultaneous particles crossing the AMS detector. Since the ACC surrounds the inner volume of the detector, it helps in checking that only one particle travels the AMS-02 from top to bottom and that no particle enters from the side of the detector. To avoid these potential side-crossing particles from contaminating an event, no more than one ACC hit is allowed in the selection. This, with the other cuts in the interaction group, guarantees that an event has a single particle track detected.

### 3.1.1 Monte-Carlo analysis

Antihelium-3 Monte-Carlo (MC) was initially studied to build the framework to identify antihelium in data. Figure 3.1 (right) shows the reconstructed mass distribution after

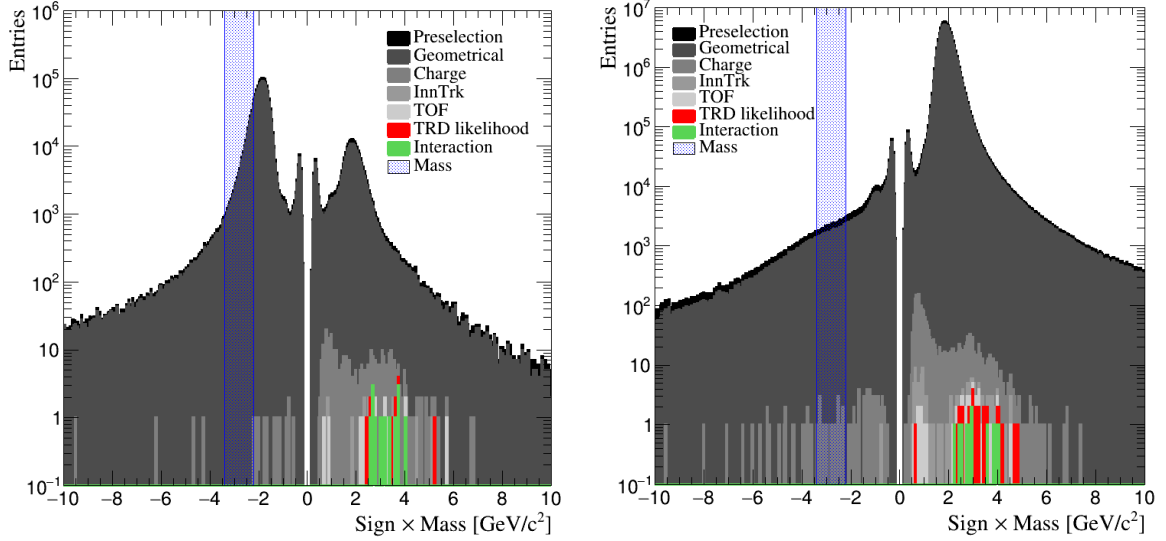


Figure 3.2 **Left:** Reconstructed mass distribution of antiproton MC multiplied by the particle charge sign. No events remain in the negative mass region. **Right:** Reconstructed mass distribution from proton MC multiplied by the particle charge sign. No events remain in the negative mass region.

applying all the cuts consecutively. The mass distribution, after all the cuts, is utilized to set the mass region where antihelium should appear. After setting the expected mass region, the acceptance from the antihelium MC is studied alongside the potential background MC. The background MC is studied simultaneously to understand the effects of the selection criteria. The acceptance is determined by dividing the generated rigidity distribution after a selection cut by the generated rigidity distribution from the MC. The acceptance also demonstrates the efficiency for the entire selection criteria as shown in Fig. 3.1 (left).

For the  $|Z|=1$  particles, a MC with  $2 \cdot 10^9$  events is used for antiprotons and  $5 \cdot 10^9$  events for protons. A MC with  $120 \cdot 10^9$  events was used for studying helium-4. A larger MC was looked at for helium because it is a particle with  $|Z|=2$  like antihelium. Figure 3.2 shows the reconstructed mass distribution for the antiproton (left) and proton (right) MC. Figure 3.3 is the reconstructed mass distribution for helium. Applying the charge cuts shows most of the  $|Z|=2$  events being suppressed. Since helium is a  $|Z|=2$  particle, it is not suppressed

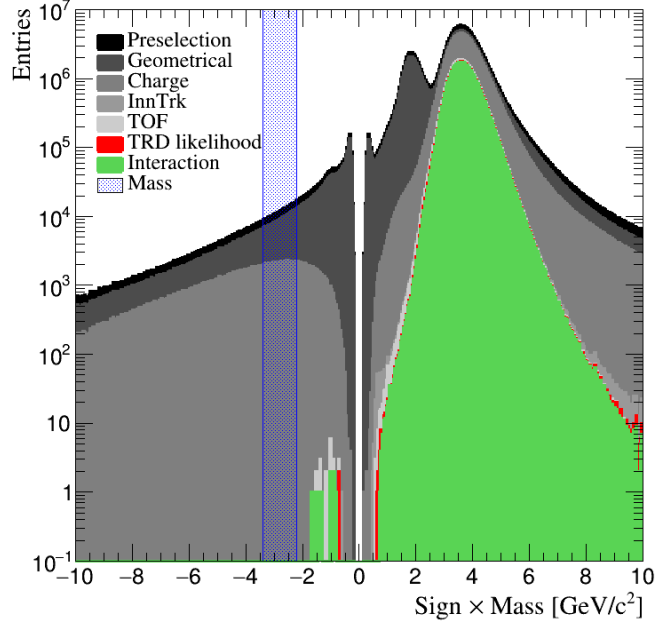


Figure 3.3 Reconstructed mass distribution from helium MC multiplied by the particle charge sign.

by the charge cut. However, the inner tracker cuts begin to increase the quality of the track and this suppresses most of the misreconstructed events which are on the negative side of the mass plot for helium. Looking at the  $|Z|=1$  particle distribution shows that all the events on the negative mass side disappear for antiproton and only a few events remain for proton. The antihelium acceptance, in Fig. 3.1 (left), shows its distribution decrease from the charge and inner tracker cuts. The acceptance is seen to decrease the most after applying the cuts from the inner tracker group. Studying the cuts individually showed that the inner pattern cut reduces the acceptance the most. This cut is important because it requires an event to hit every plane from the inner tracker. While the inner pattern reduces the efficiency of the selection it is important in suppressing misreconstructed events.

By applying the cuts in the order shown, the other cut groups do not seem to contribute as much as the inner tracker group, but this is not the case. The other quality cuts were analyzed, and they showed a comparable decrease in misreconstructed events

as the inner tracker group when applied initially. This means the other groups are just as important in removing bad tracks that could be misreconstructed as antihelium. Looking at the reconstructed mass distributions demonstrates that these cuts do help in removing even more misreconstructed events. The events that remain from the  $|Z|=1$  MCs are misidentified events that are mistaken as  $|Z|=2$  particles. The helium MC also has misreconstructed events that have been measured to have a negative rigidity. The acceptance from the antihelium MC does not decrease significantly after requiring an improvement to the quality of an event. However, the antihelium MC still shows misreconstructed events like the MC from the background being investigated. While no particles from the background MC remain in the antihelium mass region, the current selection does not completely negate bad tracks.

The misreconstructed events from the antihelium and background MC showed that there was a disparity between the generated and reconstructed rigidity values. These misreconstructed events that remain in all the MCs studied could be suppressed by using more information from the TOF, TRD, and possibly RICH. The antiproton and proton MC make it apparent that only utilizing the charge from the inner tracker and TOF is not enough to completely remove  $|Z|=1$  particles. Therefore, the charge and particle track measured by the TRD could be useful to further suppress antiprotons and protons. The number of extra hits measured on the TOF would further improve the quality of a track and this can be used to suppress the misreconstructed events from the antihelium and background MC. Studying the misreconstructed events showed that most of the bad events from the  $|Z|=1$  particles and some of the bad  $|Z|=2$  particles would be suppressed with the additional TRD and TOF variables. A ring being measured at the RICH could be an indicator that the particle measured is a high-velocity cosmic ray that has been measured incorrectly. These variables would need to be studied more to see how they could improve the selection of the

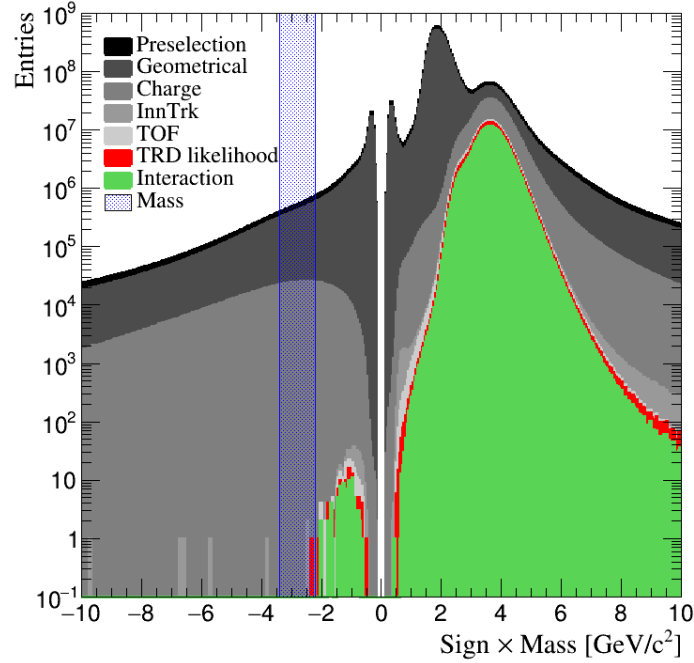


Figure 3.4 Reconstructed mass distribution for data using the selection criteria from the Standard method.

Standard method. The acceptance of the antihelium MC would need to be studied closely to continue improving its efficiency.

### 3.1.2 Data analysis and Exclusion limit

The antihelium exclusion limit is calculated to set a discovery limit with the Standard method. The exclusion limit calculated is determined like the sensitivity by:

$$S = \frac{N_{obs} - b}{AccT\Delta E}. \quad (3.2)$$

The antihelium exclusion limit is determined by using data taken between 2011 to 2021.

**Number of events**  $N_{obs}$  is the number of events in data that are observed after the entire selection criteria in the expected antihelium mass region. Figure 3.4 shows the reconstructed mass distribution from 10 years of data after applying the Standard method cuts sequentially like for the MCs. The distribution shows zero events remaining after these cuts so the exclusion limit can be calculated. The events in the negative mass region showed a difference in the reconstructed rigidity between the Kalman and Choutko methods, some had extra interactions in the TRD, and some had extra hits on the TOF. No events remaining could indicate that some cuts are too restrictive and including other variables could help in the optimization of other cuts. Applying the Standard method to the background candidate MCs showed no events being misreconstructed as antihelium. Therefore, the number of background events  $b$  is set to zero for this analysis. This value could fluctuate when determining its statistical significance. The antihelium exclusion limit is set at a 95% confidence level by using the Feldman-Cousins [69] statistical approach.  $N_{obs}$  is set to 3.09 from the Feldman-Cousins 95% confidence level signal.

**Energy region** The low-energy region searched in this analysis for antihelium utilizes the TOF's precise velocity measurement. As mentioned in section 2.2, the TOF determines the velocity of a particle ( $\beta$ ) in the range from 0.5 to 0.85. The rigidity region studied from the TOF range is determined using:

$$R = \frac{m\gamma\beta}{Z}. \quad (3.3)$$

$Z$  is the absolute charge for antihelium,  $m$  is the expected mass for antihelium,  $\beta$  is the velocity, and  $\gamma=1/\sqrt{1-\beta^2}$ . Hence, the rigidity region obtained is from 0.81 to 2.27GV. The rigidity range from 1 to 2GV is focused on for this analysis. The energy region is

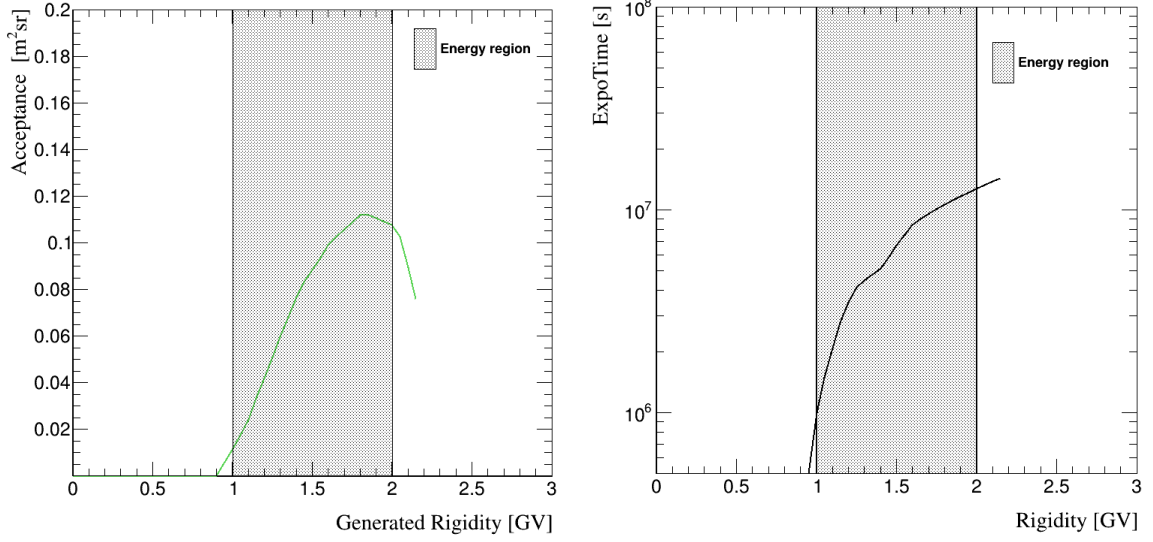


Figure 3.5 **Left:** Interpolated acceptance distribution from antihelium after entire selection. **Right:** Exposure time utilizing the IGRF geomagnetic cutoff calculation.

calculated from the velocity region using:

$$E = \frac{\sqrt{Z^2 R^2 + m^2} - m}{A}. \quad (3.4)$$

Again  $m$  is the expected mass for antihelium,  $Z$  is the absolute charge,  $R$  is the rigidity, and  $A$  is the number of nucleons for antihelium-3. Thus, with the rigidity region chosen, the energy range is from 0.21 to 0.69 GeV/ $n$ .

**Acceptance** The average acceptance ( $\overline{Acc}$ ) uses the antihelium MC acceptance distribution after the entire selection and mass cut shown in blue in Fig. 3.1. The average acceptance is determined by getting the acceptance value in the rigidity region of interest every 0.05GV as shown in Fig. 3.5 (left). The average acceptance in the region of interest is 0.077 m<sup>2</sup>sr.

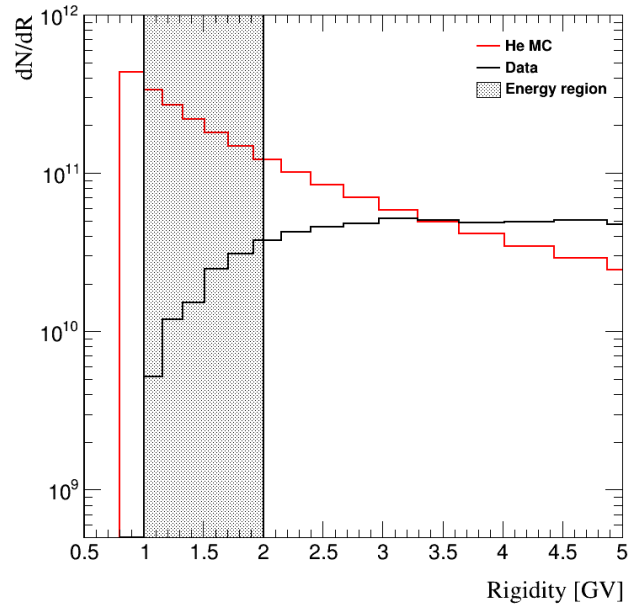


Figure 3.6 The number of events per rigidity bin from data and the helium-4 MC to demonstrate the size of the MC will properly account for the events in data.

**Exposure Time** The average exposure time ( $\overline{T}$ ) is determined like the  $\overline{Acc}$  (Fig. 3.5 (right)). The exposure time is the amount of time the detector spends with cosmic rays at certain rigidities. The exposure time is obtained from data that is above the cutoff rigidity. The cutoff rigidity describes if a charged particle with a rigidity can enter the Earth's geomagnetic field or if it is deflected. This analysis uses geomagnetic cutoff values determined by the International Geomagnetic Reference Field (IGRF) [72]. The cutoff rigidity at a position is an effective value that takes the largest value from the directions examined at a position on the magnetosphere. This value is multiplied by 1.2 for safety to not need to use a value for a direction and to account for any uncertainties in the measurements. In Chapter 4, the cutoff rigidity is discussed more. The average exposure time is  $6.896 \cdot 10^6$ s.

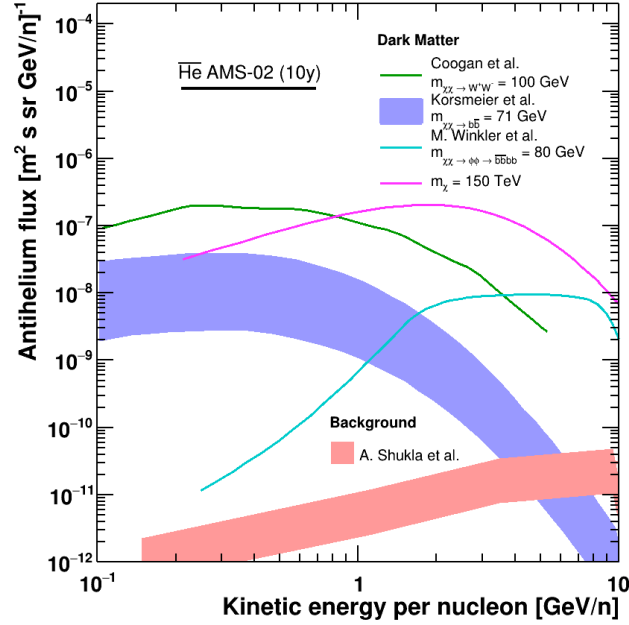


Figure 3.7 The exclusion limit obtained with Standard method for 10 years. Predicted antihelium flux from different Dark Matter models [47-50, 68] and the predicted background [51].

The number of events per rigidity for the helium MC and data is compared to show that the main source of background will properly account for data. The number of events per rigidity for data is determined by:

$$dN/dR = Flux \cdot T \cdot AccGeo. \quad (3.5)$$

The *Flux* refers to the helium flux measured by AMS, *T* is the exposure time at a rigidity bin, and *AccGeo* is the geometrical acceptance of AMS which is 47.78m<sup>2</sup>sr. Figure 3.6 shows that the helium MC statistics are large enough to explain the current number of events per rigidity bin from data. The high MC statistics can be used to study any effects that would appear in data between 1 to 2GV. This is applicable for 10 years of data being used for this analysis and with the exposure time distribution utilizing the

IGRF geomagnetic cutoff. The exclusion limit with the Standard method is  $1.2 \cdot 10^{-5}$   $(\text{GeV}/n \cdot \text{m}^2 \text{sr} \cdot \text{s})^{-1}$  with a 95% confidence level. Fig. 3.7 shows the exclusion limit for 10 years of data from AMS-02 with the predicted antihelium-3 fluxes from Dark Matter and background models [47, 48, 50, 51, 68].

## 3.2 BDT Method

Another method to search for antihelium was explored because the Standard method leaves no events remaining in the expected antihelium mass region. To make sure that the selection criteria cuts are not too restrictive, a Toolkit for Multivariate Analysis (TMVA) was explored [70]. TMVA provides an environment for parallel processing and application of multi-variable classification and multivariate regression techniques with TMVA version 4 (TMVA 4). With TMVA 4, the Boosted Decision Tree (BDT) algorithm was incorporated to select good track events to give any antihelium candidates identified confidence in the quality of the track.

A decision tree [70] is a binary tree-structured classifier that repeats yes/no decisions one variable at a time until a stop criterion is fulfilled. The phase space created from the variable is split into multiple regions that are then classified as signal or background properties. A Boosted Decision Tree is the culmination of multiple decision trees, which make a forest. The trees are weighted and combined into a single classifier that denotes the signal and background percentage (will be referred to as BDT value). The BDT will be trained to continue suppressing any background events with the training and testing provided by TMVA 4. Additionally, the BDT should improve the antihelium acceptance with its optimization of cutting on the variables being used.

Table 3.2 Initial cuts, from standard methods selection criteria, applied to data used to train BDT.

Variable	Cut		Group
Physics trigger	=	1	Preselection cut
Velocity ( $\beta$ )	>	0.5 < 0.85	Preselection cut
Tracker Layer 2 theta		< 45	Geometrical cut
Tracker theta (at Z=-100cm)		< 45	Geometrical cut
Tracker radial distance (at Z=-100cm)		< 80	Geometrical cut
In Tracker Layers	$\geq$	1	Geometrical cut
Inner Tracker Charge	>	1.7 < 2.7	Charge cut
UTOF Charge	>	1.7 < 2.7	Charge cut
LTOF Charge	>	1.7 < 2.7	Charge cut
Inner Pattern	=	1	Inner tracker cut
TRD Electron Helium Log Likelihood	$\geq$	0.4	TRD Likelihood cut

### 3.2.1 BDT training with data

The BDT utilized in this analysis works to separate good (signal) and bad (background) tracks by the mass of an event. The BDT uses a small sample of data to build the technique to select good tracks. The good tracks are defined as being in the mass region between 3.5 and 3.7  $\text{GeV}/c^2$  and bad tracks are events that have a mass larger than 6  $\text{GeV}/c^2$ . The mass region for the good tracks is where helium is expected and it was chosen based on the low background contamination from  $|Z|=1$  particles. Helium has the second-largest abundance in CRs and the same absolute charge as antihelium. The mass from helium is not near the reconstructed mass expected for antihelium so this will remove bias that could occur when checking the complete data set for antihelium. The mass region for the bad tracks is away from the expected helium mass so they would be misreconstructed helium. The BDT is trained from data events that remain after applying the initial cuts in Tab. 3.2. The initial set of cuts applied are identifiers for a  $|Z|=2$  particle and for events to have a minimum quality for the track. This is why the bad tracks can be treated as misreconstructed helium. As described in section 3.1 for the Standard method, the cuts on charge and TRD likelihood

are useful for selecting particles with  $|Z|=2$ . The other cuts that are shown in Tab. 3.2 are to ensure a particle is passing through the detector while remaining inside its volume.

The BDT is trained with the quality track variables in Tab. 3.1 from the interaction group, TOF group, and most of the inner tracker group. From the total number of events available from the sample, the events are separated initially based on their mass. After separating the events into each group of signal or background, the events in the group are split in half. The BDT takes one-half of each of the groups to begin its training and checks the values for the variables input for training. The training uses the TMVA 4 parallel processing to apply the BDT algorithm. The BDT is separating a variable into being signal or background by essentially asking many yes or no questions. TMVA 4 ranks the variables in this process on how important their value is for an event to be classified as signal or background. Once this part of the training is complete the other half of both groups are tested to verify how well the events are separated. A new ranking list with values is given for the variables trained that are likely to correspond to a good or bad track. TMVA 4 creates various plots for the BDT that demonstrate the separation between good (signal) and bad (background) tracks as shown in Fig. 3.8.

Figure 3.8 shows the signal and background efficiency as a function of the value from the BDT. From this plot a minimum BDT value is selected based on the signal and background efficiency values. The BDT value that has a high signal efficiency with a low background efficiency is chosen to be the minimum BDT value that will be cut on. A minimum cut on the BDT value is chosen at 0.08 because the background and signal efficiency are roughly 0.05 and 0.8 respectively. This minimum cut accompanies the initial cuts in Tab. 3.2, and this is referred to as the BDT method.

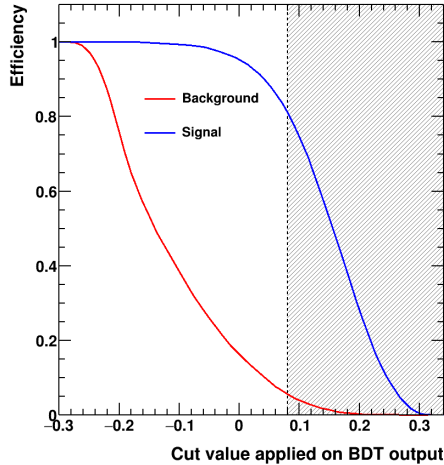


Figure 3.8 Signal (blue) and background (red) efficiency as a function of the BDT value.

### 3.2.2 MC with BDT

The antihelium and background MC are examined with the established BDT method built from data. Figure 3.9 shows the reconstructed mass using the BDT methods selection and includes the Standard methods distribution for comparison. Fig. 3.9 shows the acceptance after the BDT method with the cut on the expected mass region to properly compare with the Standard methods acceptance distribution. These figures show that the BDT method is comparable to the Standard method. The average antihelium MC acceptance from the BDT method is  $0.089 \text{ m}^2\text{sr}$ . The acceptance using the BDT method shows a 15.6% increase from the Standard method's value.

Next is checking the MC from potential background to ensure the background remains suppressed. The antiproton and proton MC reconstructed mass distributions are in Fig. 3.10. Like the Standard method, the  $|Z|=1$  particles are suppressed from being misreconstructed as antihelium. Figure 3.11 shows the mass distribution from the helium MC and no helium remains in the antihelium mass region. Like the reconstructed mass distribution with the Standard method, there are some misreconstructed events in the

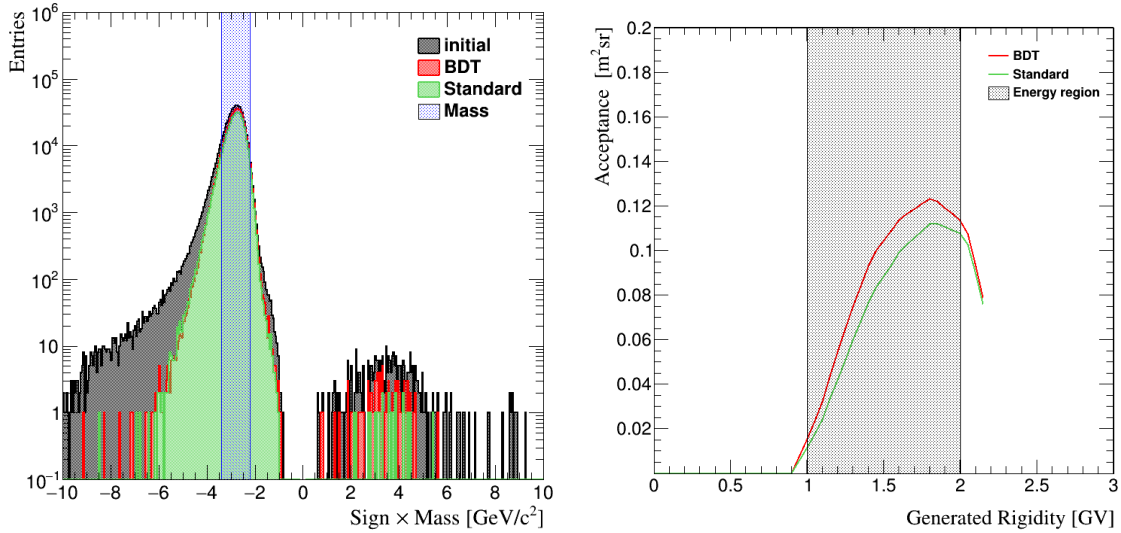


Figure 3.9 **Left:** Reconstructed mass distribution for antihelium MC with the BDT method. **Right:** Antihelium MC acceptance that has comparison between BDT and Standard method. BDT includes the cut on mass like in Fig. 3.1.

antihelium and background MC. Since the BDT method was able to improve the average antihelium acceptance and continue to suppress the background MC; the improvements that were discussed in section 3.1.1 could be utilized in the BDTs training. Using the particle track and charge information from the TRD, and the number of extra hits measured on the TOF could improve the BDTs selection when applied to the MC. The measurement of a ring at the RICH is another component that could verify the type of event that is being measured. These variables could help the BDTs training and help with its selection.

### 3.2.3 Data with BDT

After applying the BDT on the antihelium and background MC, the complete data set analyzed in the Standard method is analyzed with the BDT method. Figure 3.12 shows the mass distribution from data with the result from the Standard method to compare. Three events from data remain with the BDT method. The properties of these events are checked

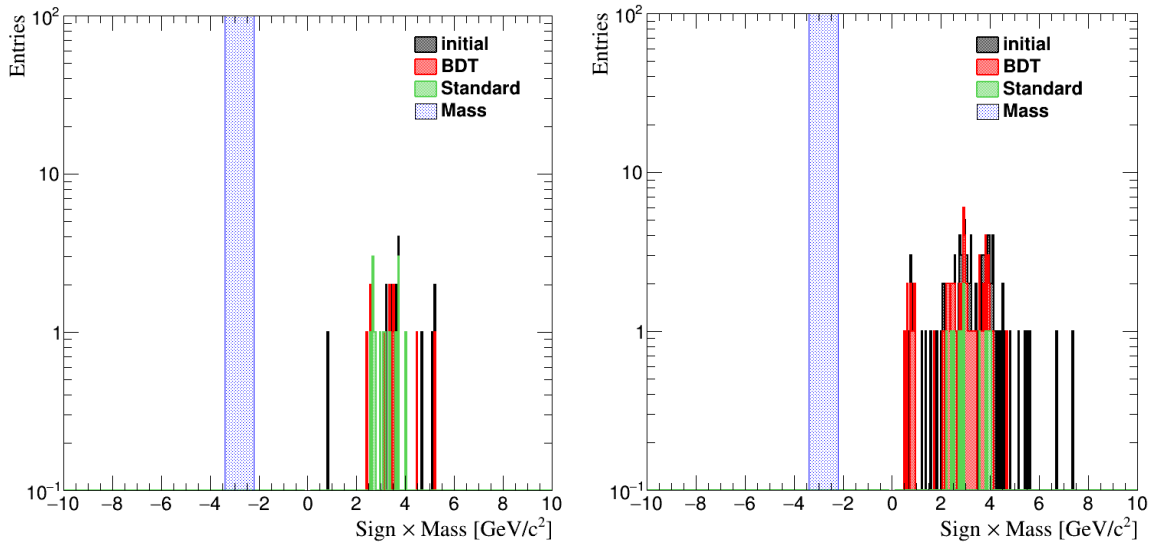


Figure 3.10 **Left:** Reconstructed mass distribution for antiproton MC with the BDT method. **Right:** Reconstructed mass distribution for proton MC with the BDT method.

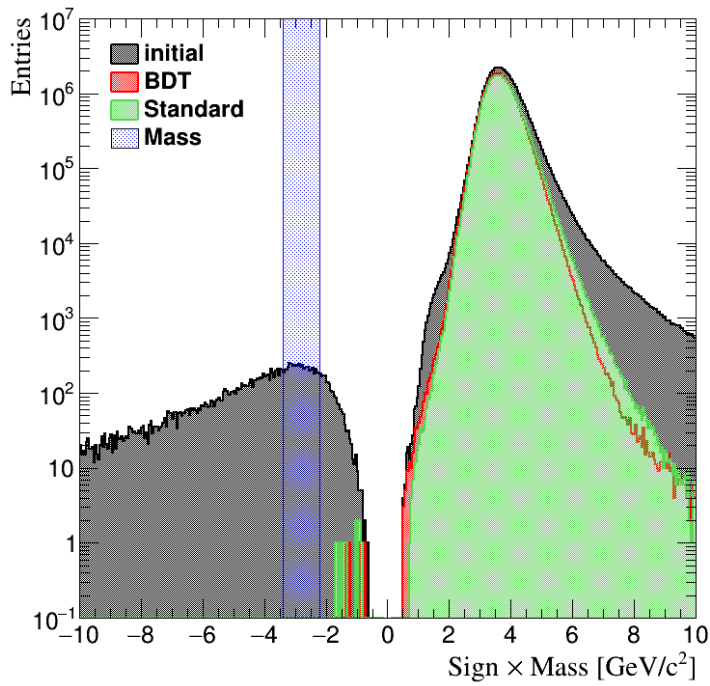


Figure 3.11 Helium MC reconstructed mass distribution with the BDT method.

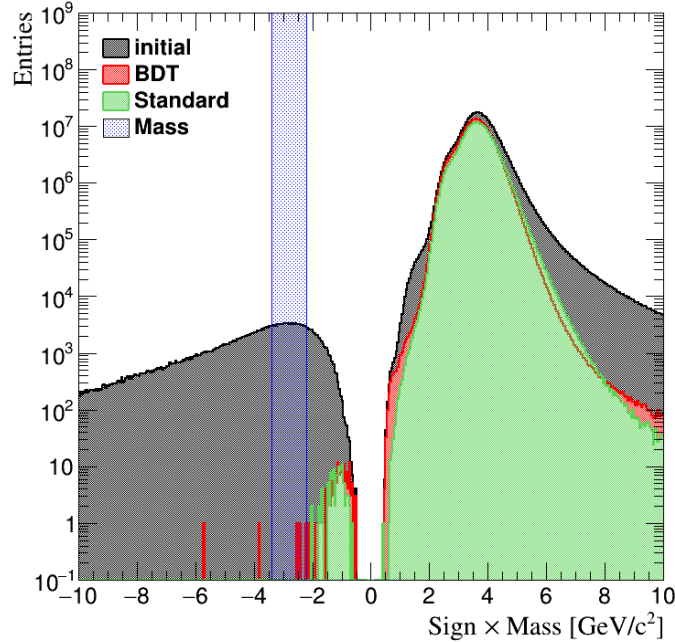


Figure 3.12 Reconstructed mass distribution for data with the BDT method.

to understand why they do not appear in the Standard method. Looking into this reveals that all the events have a bad value for at least one quality track variable. An event display for one of the three events is shown in Fig. 3.13. This event has a bad  $\chi^2$  value in the bending plane ( $Y$ ) from the Choutko algorithm. Figures 3.14 and 3.15 are the other two events from data that were observed in the antihelium mass region. The second event had two particle tracks measured and the third event had two hits on the ACC. These events would need to be investigated further. Including the additional information from the sub-detectors discussed could improve the BDTs ability to choose better-quality tracks and learn more about the events observed.

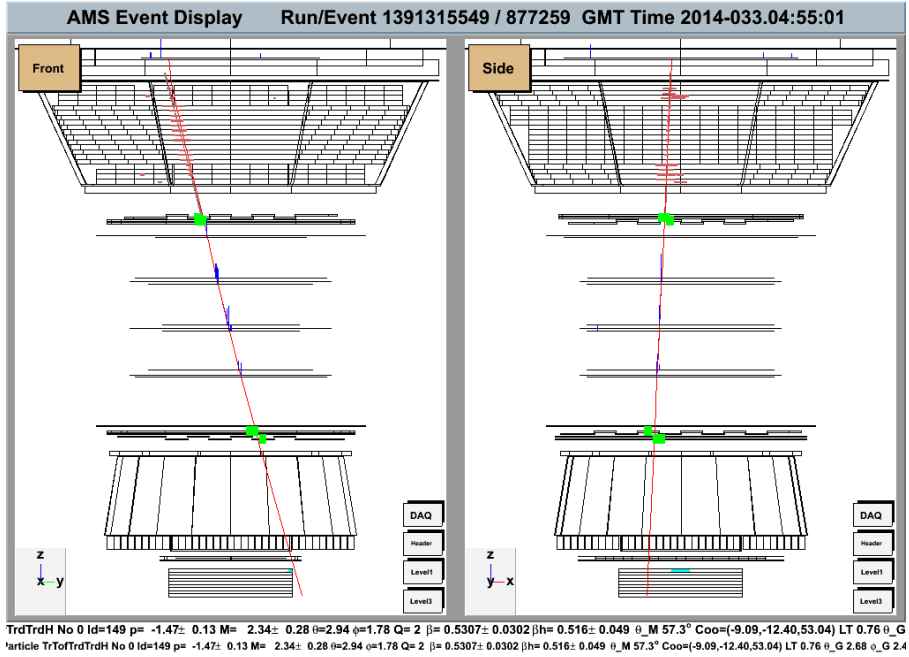


Figure 3.13 Event display of one event in data that remains after BDT cut. Event has a bad  $\chi^2 Y$  value with the Choutko algorithm.

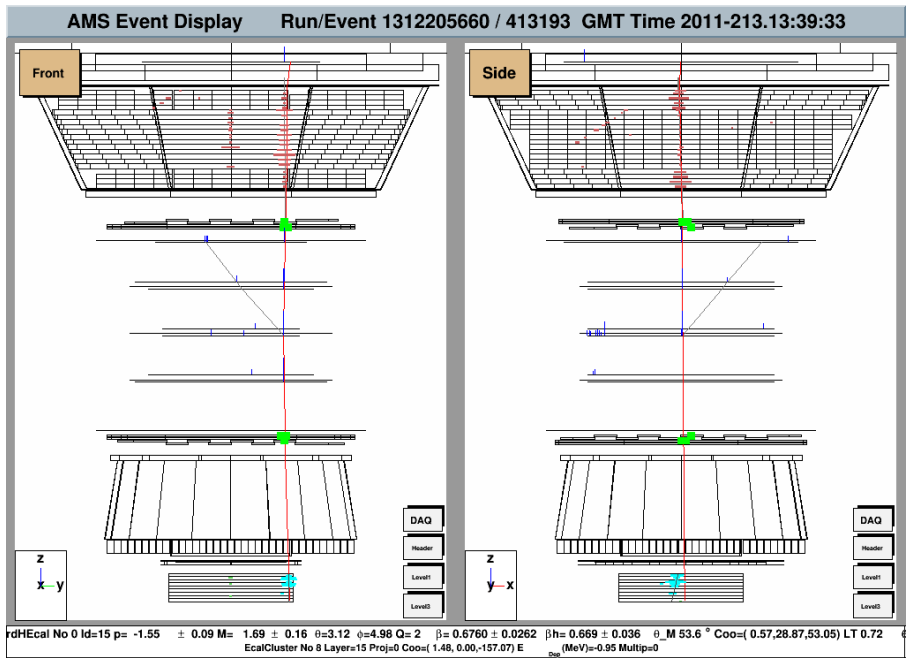


Figure 3.14 Event display of second event in data that remains after BDT cut. Event had two particle tracks measured.

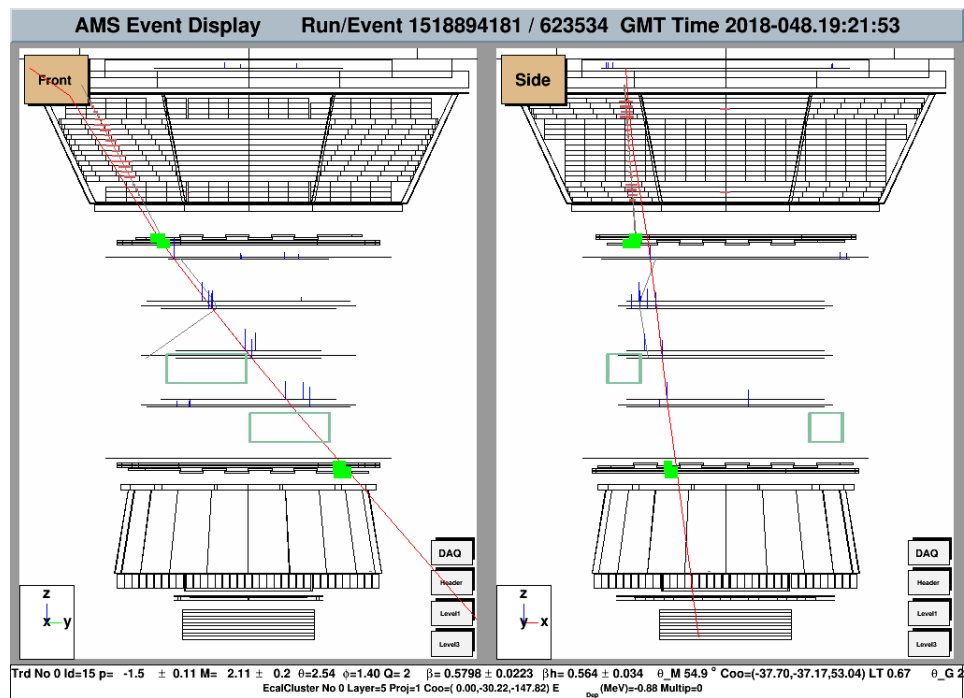


Figure 3.15 Event display of third event in data that remains after BDT cut. Event had two hits on the ACC.

# Chapter 4

## Geomagnetic Cutoff Rigidity

Cosmic Rays are highly abundant, and their origin is difficult to discern. Any CRs that come to Earth will experience the Lorentz Force caused by the Earth's magnetic field. The rigidity value where particles are either deflected away or enter the Earth's geomagnetic field at a particular point is known as the cutoff rigidity [71]. The measured rigidity of a particle is checked to be above the cutoff rigidity to distinguish between Galactic CRs and albedo space radiation. Galactic CRs are cosmic rays that come from outside the Earth's magnetosphere and are above cutoff. Albedo space radiation is another class of CRs that are created by the Galactic CRs interacting with the Earth's atmosphere. These CRs are unable to escape the Earth's magnetosphere and can collide with the atmosphere again before they decay [71].

AMS-02 uses the IGRF magnetic model for the cutoff rigidity and applies a factor of 1.2 to the cutoff value for safety. This is done so the cutoff does not need to be computed for a specific direction. By doing this some low-rigidity cosmic rays will be passed over. Since AMS-02 is aboard the ISS, it already covers a few regions where low-rigidity cosmic rays are plentiful. Therefore, the AMS-02 exposure time at low rigidities is reduced which affects the study of antihelium. A new method of calculating the geomagnetic cutoff will

be done with PLANETOCOSMICS. This technique will obtain a cutoff value that depends on the direction and position to improve the exposure time at low rigidities.

## 4.1 PLANETOCOSMICS

The PLANETOCOSMICS [74] software is a simulation framework that computes the propagation of charged particles in the magnetosphere, computes the flux of particles created by the interaction between cosmic rays with the planet's atmosphere, computes the energy deposited by cosmic ray showers in the planet's atmosphere, and visualizes the trajectories of primary and secondary particles in the environment. Models for the magnetic field and atmosphere can be incorporated into the PLANETOCOSMICS framework, and the magnetic field used for simulations has an internal and external field component [72]. The internal field from the internal sources of a planet is implemented into the simulation with the IGRF magnetic field model that uses the magnetic field measurements that are provided by the *International Association of Geomagnetism and Astronomy* [72]. The external field incorporates the Tsyganenko and Sitnov [75], TSY04, magnetosphere model. The TSY04 model was included by von Doetinchem and Yamashiro [76] into PLANETOCOSMICS and it accounts for the influence of charged particles that the sun emits from its solar wind on the magnetic field which increases at higher altitudes [77].

A back-tracing method is used for verifying whether a particle's track is allowed or forbidden. The particle is traced backward from a starting point inside the Earth's magnetic field and the path of the particle is tracked from an initial direction and rigidity as seen in Fig. 4.1. A track is labeled as allowed if the particle travels through the magnetic field (purple line in figure) and a track is forbidden if it remains trapped by the magnetic field (red line in figure).

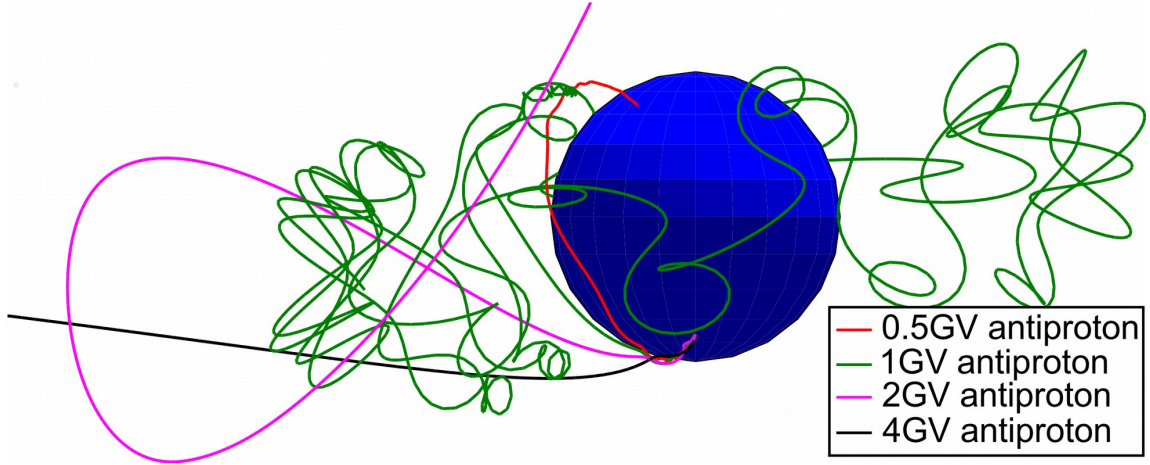


Figure 4.1 Visual by PLANETOCOSMICS of tracks being back traced at a position for a direction at different rigidity values.

The original method of obtaining a cutoff value would check rigidities in linear steps of 0.1GV from 0.1 to 100GV. This would provide  $R_L$ ,  $R_U$ , and  $R_C$  for a direction.  $R_L$  and  $R_U$  are the rigidity values that represent the lowest and highest computed forbidden  $\rightarrow$  allowed transitions.  $R_C$  is the effective cutoff rigidity and is determined by:

$$R_C = R_U - n_{allowed}\Delta R. \quad (4.1)$$

$\Delta R$  is the uniformly spaced rigidity intervals and  $n_{allowed}$  is the number of allowed rigidities found between  $R_L$  and  $R_U$ . Therefore,  $R_C$  contains information about  $R_L$  and  $R_U$  and satisfies the inequality  $R_L \leq R_C \leq R_U$ . AMS-02 uses the maximum  $R_C$  for an area of directions examined at a position and multiplies it by a safety factor of 1.2 to consider any small changes or uncertainties in the measured rigidity. By using this safety factor, the cutoff rigidity for a certain direction is not being considered and would neglect smaller rigidities than the maximum cutoff value.

Table 4.1 Direction and position binning that is used for the cutoff rigidity analysis.

variable	range	step size
sin(latitude)	-1–1	0.1
longitude	0–360°	20°
azimuth	0–360°	20°
cos(zenith)	-0.2–1	0.1

## 4.2 Cutoff Analysis

This new technique will be considering the position and direction for the cutoff rigidity calculation. The starting position of a particle is described by the altitude, latitude, and longitude on the Earth. The incoming direction of a particle is described by the zenith and azimuth angle at the starting position. Table 4.1 shows the parameters for the directions and positions that are used for this analysis. The sine of the latitude is employed to check the positions near the equator more than at the poles because the path of the ISS is around the Earth’s equator, within the latitude of 51.6°. The directions being investigated go below zero for the cosine of zenith because tracks could arrive at a given position from below the local horizon and be allowed as shown in Fig. 4.2 (left). For this analysis, the geomagnetic cutoff will be determined during the period that the AMS-02 on the ISS, starting with its installation on May 19, 2011.

A geomagnetic cutoff value is determined at a given position for any incoming direction. The new method explores rigidities in a logarithmic scale from 0.1 to 100GV (100 to 100,000MV) and provides a histogram per direction analyzed as shown in Fig. 4.3 (started by Ref. [73]). The minimum and maximum rigidity are converted to log scale with  $\log_{10}(R)$  and there are 75 bins between the extremes. The probability of a forbidden track for the histogram is determined by checking 50 different rigidity values within a bin. The forbidden probability values are calculated by taking the ratio of rigidity values that

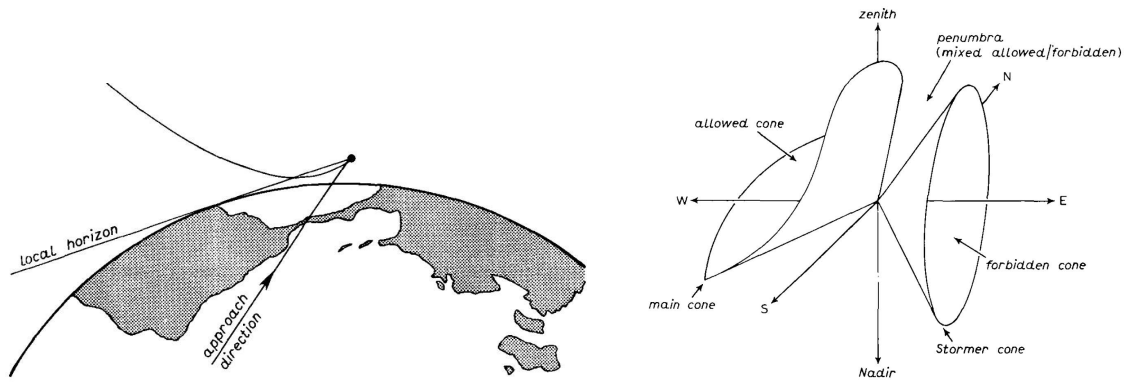


Figure 4.2 **Left:** Trajectory of a particle reaching the starting position from a direction that is below the local horizon. **Right:** Example of how a circular cone at a position in the magnetosphere would look for a rigidity  $R$  (right cone is forbidden cone). Images from Ref. [78]

are forbidden and dividing them by the number of values checked. The new method starts by checking the bin that contains the Størmer cutoff rigidity and then analyzing the larger rigidity values. The Størmer cutoff rigidity refers to Carl Størmer’s [79] definition, that at any point in a dipole magnetic field there exists a circular conical shell of directions that are forbidden for rigidities smaller than  $R$  as depicted in Fig. 4.2 (right). This means that at a chosen position in the magnetosphere and for a fixed direction there is a “forbidden cone” with a Størmer cutoff rigidity ( $R_S$ ). The Størmer cutoff rigidity is the rigidity  $R$  where all the trajectories are forbidden for smaller rigidity values than  $R_S$  because they are within the forbidden cone. Once all the larger values than  $R_S$  are studied, the smaller rigidity values are looked at. This new method assumes that if there are three consecutive bins to the right (left) of the starting bin, with a forbidden probability of exactly zero (one) then all the larger (smaller) rigidities will have that probability. This is assumed from the discussion of the forbidden cone that contains an  $R_S$  for any direction. To ensure this assumption does not set the probability for an entire region of rigidities that may have a different at a larger or smaller value, some larger and smaller rigidity bins are analyzed for a few values. If the probability from the small sample is not zero (one) then all the bins up to that rigidity

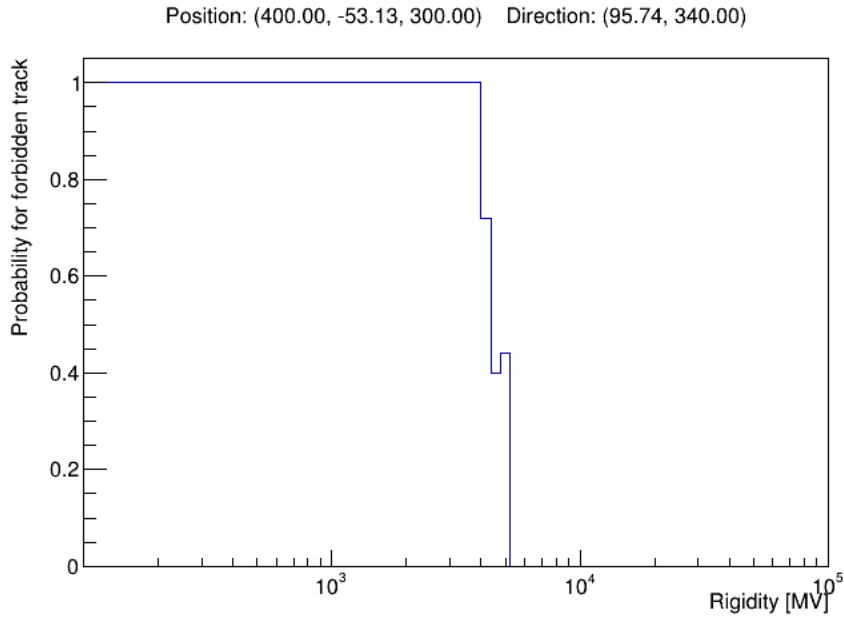


Figure 4.3 Forbidden probability histogram for a position (altitude [km], latitude [deg], longitude [deg]) and direction (zenith [deg], azimuth [deg]).

value are analyzed normally. Another detail with this new method is that if a forbidden probability is not zero or one then 3 times as many rigidity values in that bin are looked at to get a more accurate probability value. This is done to make the computation more efficient, by not requiring a large number of rigidity values to be checked for every bin.

The cutoff rigidity for a direction is obtained by finding the rigidity value that is below a forbidden probability and the larger rigidity values remain below that forbidden probability. The cutoff rigidity value for Fig. 4.4 with an allowed probability of 100% (probability of forbidden track is zero) would be approximately 0.72GV. The dashed lines in the plot show the original method's effective cutoff multiplied by a factor of 1.2 for each direction shown. This demonstrates that multiplying the effective cutoff by a safety factor excludes some low-rigidity CRs. This safety factor is applied to the largest effective cutoff at a position, so the current cutoff that AMS-02 uses does not consider the direction of a particle. Thus,

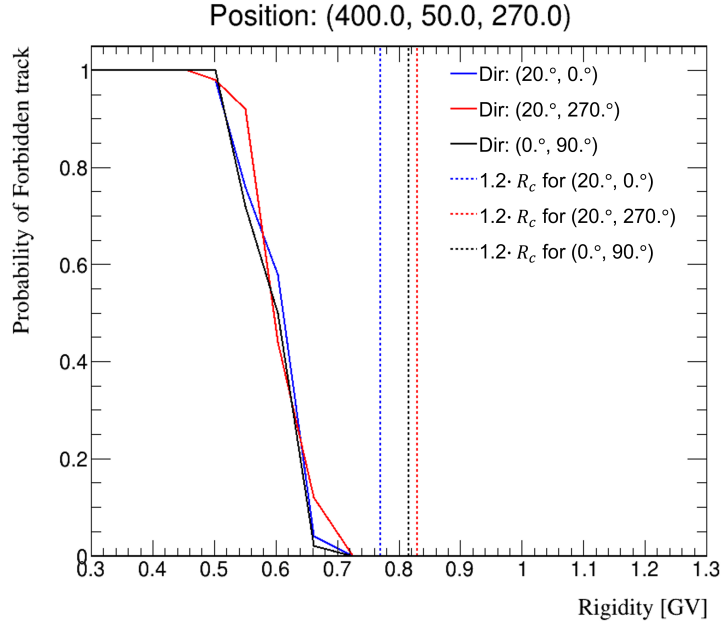


Figure 4.4 Forbidden probability plot used to get more accurate cutoff rigidity value. Dashed lines show the effective cutoff rigidity obtained by original method.

this new method can incorporate direction-specific cutoff values to improve the exposure time at low-rigidity regions being explored by antinuclei studies.

By checking all the directions mentioned in Tab. 4.1, the cutoff rigidity values can be plotted onto a histogram for a position as shown in Fig. 4.5 (left). This step is repeated for all the positions on the Earth being checked to create a map of the average cutoff rigidity as shown in Fig. 4.5 (right).

The next step that this work can do is to have these cutoff rigidity maps every 100 days from the installation of the AMS-02 on the ISS. Determining the improvement that would be caused by using the cutoff rigidity calculated with the new method. This would provide Figure 4.2 shows the cutoff rigidity map for the first day on May 19, 2011. Using the new method described the cutoff rigidity can improve the exposure time for the low-energy region explored for antinuclei by experiments like AMS-02.

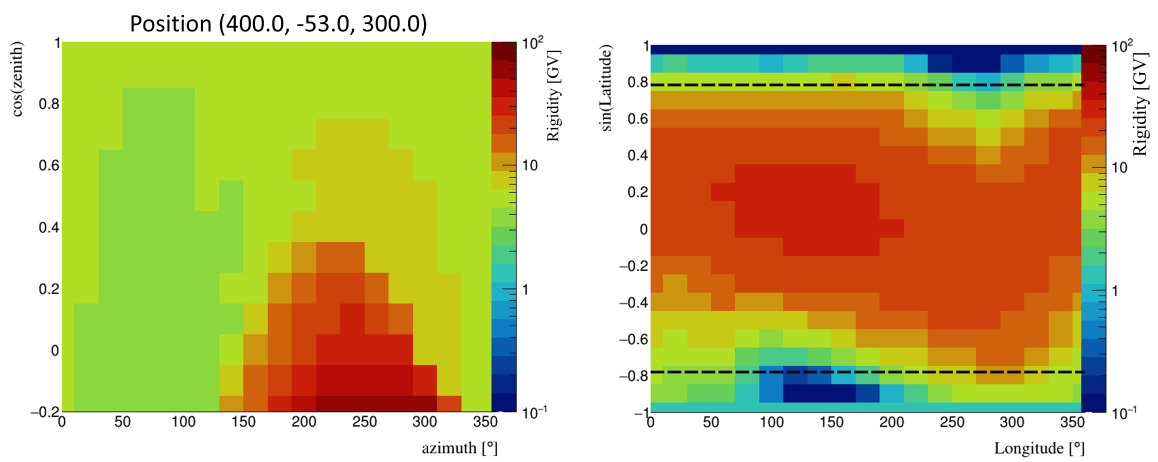


Figure 4.5 **Left:** Cutoff rigidity, with 100% allowed tracks, histogram created by looking at all directions for a position. **Right:** Cutoff rigidity map for May 19, 2011, for 100% allowed tracks. The black dashed lines demonstrate a  $|\text{Latitude}| < 51.6^\circ$  which the ISS travels.

# Chapter 5

## Conclusion

### 5.1 AMS-02 Antihelium Exclusion limit

This work discussed the importance of searching for antihelium in cosmic rays at low energies as an indicator for new physics. The research focused on creating a method for identifying antihelium in a low-energy region with AMS-02. Analyzing MC simulations was the first step in creating a framework to search for antihelium candidates. The MC from antihelium was used to provide the efficiency for the implemented selection criteria and to set a region in mass where cosmic antihelium are expected. The helium MC was used to check how the main source of background would be suppressed with the cuts applied. The antiproton and proton MCs were studied to check that they are properly suppressed by the resolution of the charge obtained by the Inner Tracker and the TOF. Two methods to identify antihelium were utilized for this work.

The standard cut method utilized to search for antihelium showed that no events from the helium MC would appear in the expected antihelium mass region. The average acceptance from the antihelium MC in the energy region of 0.21 to 0.69 GeV/n was  $0.077\text{m}^2\text{sr}$ . The data checked with the standard method showed no cosmic ray events remaining in the expected antihelium mass region. The exclusion limit with a 95%

confidence level was calculated to equal  $1.2 \cdot 10^{-5} \text{ (GeV/n} \cdot \text{m}^2 \cdot \text{sr} \cdot \text{s)}^{-1}$  with Feldman-Cousins statistics.

A Boosted Decision Tree algorithm was explored as a method to select good antihelium candidates after applying some initial cuts that are identifiers  $|Z|=2$  particles. The BDT was trained to pick the best quality tracks for  $|Z|=2$  particles. Results from the BDT method showed the average acceptance to equal  $0.089 \text{m}^2 \cdot \text{sr}$  which is an increase of 15.6% in comparison to the standard method. The BDT method could suppress the background from the helium MC and leave three potential antihelium events in the data. These events in data all had at least one quality track variable that would be unfavorable.

### **Next Steps in Antihelium analysis**

The Standard method left misreconstructed events after applying the entire selection criteria in antihelium, helium, antiproton, and proton MC. The events remaining in the antiproton and proton MC are on the positive side of the reconstructed mass plots. The helium MC had a few events remaining on the negative side of the reconstructed mass plot. The antihelium MC showed a few events remaining on the positive side of the reconstructed mass plot. These misreconstructed events all had the same issue where the generated and reconstructed rigidity values are different. Including the number of tracks from the TRD, the charge from the TRD, and the number of extra hits from the TOF would suppress most of the misreconstructed antiproton and proton MC events. This information would remove some of the antihelium and helium MC events. The RICH could also be useful in ensuring that a Cherenkov ring is not created. This would be important in verifying the type of particle that is being measured. The Standard Method could then modify some of the other quality track variables to improve their efficiency and selection for identifying antihelium in data. The Standard Method could then modify some of the other quality track variables to improve the efficiency of the antihelium acceptance and for identifying antihelium in data.

The BDT method showed an improvement in the average antihelium acceptance and left some events in the data, but it also showed misreconstructed events in all the MC samples. The misreconstructed events in the MC samples had the same issues as those discussed for the Standard method, where the generated and reconstructed values were different. Including the additional information from the TOF, TRD, and RICH would be beneficial in the BDTs training. Since the BDT was trained with the variables used in the Standard method then it could be used to optimize its selection with these additional variables.

## 5.2 Cutoff Rigidity

The geomagnetic cutoff was studied to better understand the cutoff rigidity for low-energy antinuclei studies. This work began by implementing a new method of checking the rigidity values for particles at a given position and incoming direction. Figure 4.4 showed that the new method of obtaining the cutoff rigidity is better for allowing more lower rigidities compared to the effective cutoff that is multiplied by a safety factor. By using direction-specific cutoff values, the exposure time can be improved for low-energy antinuclei studies by experiments like AMS-02. The cutoff analysis was able to properly run for May 19, 2001, the first day of AMS-02 operation, as shown by Fig. 4.2. The next steps for this work would be to check other dates during the AMS-02 flight time with the new method and to quantify the improvements from this new method.

## References

- [1] V. Poulin *et al.* Where do the AMS-02 antihelium events come from. [Phys. Rev. D](#) 99, 023016 (2019).
- [2] P. von Doetinchem *et al.* Cosmic-ray antinuclei as messengers of new physics: status and outlook for the new decade. [Journal of Cosmology and Astroparticle Physics](#) 2008 (2020) 035.
- [3] J.-H. Ha, D. Ryu and H. Kang. Modeling of Cosmic-Ray Production and Transport and Estimation of Gamma-Ray and Neutrino Emissions in Starburst Galaxies. [arXiv:2008.06650](#) [astro-ph.HE] (2020).
- [4] R. L. Golden *et al.* Evidence for the Existence of Cosmic-Ray Antiprotons. [Phys. Rev. Lett.](#), 43:1196-1199 (1979).
- [5] E. A. Bogomolov, N. D. Lubyayaya, V. A. Romanov, S. V. Stepanov, and M. S. Shulakova. a Stratospheric Magnetic Spectrometer Investigation of the Singly Charged Component Spectra and Composition of the Primary and Secondary Cosmic Radiation. [International Cosmic Ray Conference](#), 1:330 (1979).
- [6] O. Adriani *et al.* An anomalous positron abundance in cosmic rays with energies 1.5-100 GeV. [Nature](#), 458:607-609 (2009).

- [7] O. Adriani *et al.* A statistical procedure for the identification of positrons in the PAMELA experiment. [Astroparticle Physics](#), 34(1):1-11 (2010).
- [8] O. Adriani *et al.* Measurement of the flux of primary cosmic ray antiprotons with energies of 60 MeV to 350 GeV in the PAMELA experiment. [JETP Letters](#), 96(10):621-627 (2013).
- [9] A. A. Abdo *et al.* Measurement of the Cosmic Ray  $e^+ + e^-$  Spectrum from 20 GeV to 1 TeV with the Fermi Large Area Telescope. [Phys. Rev. Lett.](#), 102:181101 (2009).
- [10] M. Ackermann *et al.* Measurement of Separate Cosmic-Ray Electron and Positron Spectra with the Fermi Large Area Telescope. [Phys. Rev. Lett.](#), 108:011103 (2012).
- [11] J. Chang *et al.* An excess of cosmic ray electrons at energies of 300-800 GeV. [Nature](#), 456:362-365 (2008).
- [12] F. Aharonian *et al.* Energy Spectrum of Cosmic-Ray Electrons at TeV Energies. [Phys. Rev. Lett.](#), 101:261104 (2008).
- [13] F. Aharonian *et al.* Probing the ATIC peak in the cosmic-ray electron spectrum with H.E.S.S. [Astronomy and Astrophysics](#), 508:561-564, (2009).
- [14] M. Aguilar *et al.* First Result from the Alpha Magnetic Spectrometer on the International Space Station: Precision Measurement of the Positron Fraction in Primary Cosmic Rays of 0.5-350 GeV. [Phys. Rev. Lett.](#), 110:141102, (2013).
- [15] M. Aguilar *et al.* Antiproton Flux, Antiproton-to-Proton Flux Ratio, and Properties of Elementary Particle Fluxes in Primary Cosmic Rays Measured with the Alpha Magnetic Spectrometer on the International Space Station. [Phys. Rev. Lett.](#), 117:091103 (2016).

- [16] CERN website. [Latest results from the AMS experiment](#), 2018.
- [17] T. Aramaki *et al.* Review of the theoretical and experimental status of dark matter identification with cosmic-ray antideuterons. [Phys. Rep.](#), 618:1-37 (2016).
- [18] V. F. Hess. Über Beobachtungen der durchdringenden Strahlung bei sieben Freiballonfahrten. [Phys. Z.](#) 13, 1084-1091 (1912).
- [19] Mario Bertolotti. *Celestial Messengers. Cosmic Rays: The Story of a Scientific Adventure.* Springer-Verlag, Berlin, 2013.
- [20] Todor Stanev. *High Energy Cosmic Rays.* [Springer-Verlag](#), Berlin Heidelberg, 2 edition, 2010.
- [21] Claus Grupen. *Astroparticle Physics.* [Springer-Verlag](#), Berlin Heidelberg, 2005.
- [22] M. Aguilar *et al.* Precision Measurement of the Proton Flux in Primary Cosmic Rays from Rigidity 1 GV to 1.8 TV with the Alpha Magnetic Spectrometer on the International Space Station. [Phys. Rev. Lett.](#) 114, 171103 (2015).
- [23] M. Aguilar *et al.* Precision Measurement of the Helium Flux in Primary Cosmic Rays of Rigidities 1.9 GV to 3 TV with the Alpha Magnetic Spectrometer on the International Space Station. [Phys. Rev. Lett.](#) 115, 211101 (2015)
- [24] L. Accardo *et al.* High Statistics Measurement of the Positron Fraction in Primary Cosmic Rays of 0.5-500 GeV with the Alpha Magnetic Spectrometer on the International Space Station. [Phys. Rev. Lett.](#), 113:121101 (2014).
- [25] Z. Li *et al.* Precision Measurement of Positron Fraction and Combined Positron Electron Flux by AMS. [ICHEP2018 SEOUL](#) (4-11 July 2018) Indico.

- [26] M. Aguilar *et al.* Towards understanding the origin of cosmic-ray positrons. [Phys. Rev. Lett.](#), 122:041102 (2019).
- [27] O. Adriani. PAMELA Measurements of Cosmic-Ray Proton and Helium Spectra. [Science](#) 332, 69-72 (2011).
- [28] O. Adriani *et al.* An anomalous positron abundance in cosmic rays with energies 1.5-100 GeV. [Nature](#), 458(7238):607-609, (2009).
- [29] Yoon, Y. S. *et al.* Cosmic-ray Proton and Helium Spectra from the First CREAM Flight. [The Astrophysical Journal](#) 728, 122 (2011).
- [30] Carl D. Anderson. The Positive Electron. [Phys. Rev.](#), 43:491-494, Mar 1933.
- [31] Owen Chamberlain, Emilio Segre, Clyde Wiegand, and Thomas Ypsilantis. Observation of antiprotons. [Phys. Rev.](#), 100:947-950, Nov 1955.
- [32] Dorfan, D. E., Eades, J., Lederman, L. M., Lee, W. and Ting, C. C. Observation of Antideuterons. [Phys. Rev. Lett.](#) 14, 1003-1006 (1965).
- [33] T. Aramaki *et al.* Review of the theoretical and experimental status of dark matter identification with cosmic-ray antideuterons. [Phys. Rep.](#) 618 (2016): 1-37.
- [34] K. Garrett and G. Duda. Dark Matter: A Primer. [Advances in Astronomy](#), 2011:968283 (2011).
- [35] Bing-Lin Young. A survey of dark matter and related topics in cosmology. [Frontiers of Physics](#), 12(2):121201 (2016).
- [36] D. Maity and P. Saha. Connecting CMB anisotropy and cold dark matter phenomenology via reheating. [Phys. Rev. D](#) 98, 103525 (2018).

- [37] J. H. Oort. The force exerted by the stellar system in the direction perpendicular to the galactic plane and some related problems. [Bulletin of the Astronomical Institutes of the Netherlands](#), 6:249, August 1932.
- [38] F. Zwicky. Die Rotverschiebung von extragalaktischen Nebeln. [Helvetica Physica Acta](#), 6:110-127, 1933.
- [39] F. Zwicky. On the Masses of Nebulae and of Clusters of Nebulae. [Astrophysical Journal](#), 86:217, October 1937.
- [40] V. C. Rubin. Dark matter in spiral galaxies. [Scientific American](#), 248:96-106, June 1983.
- [41] T. S. van Albada, J. N. Bahcall, K. Begeman, and R. Sancisi. Distribution of dark matter in the spiral galaxy NGC 3198. [Astrophysical Journal](#), 295:305-313 (1985).
- [42] [NASA - NASA Hubble Space Telescope Detects Ring of Dark Matter - Multimedia Page](#).
- [43] D. Clowe *et al.* A direct empirical proof of the existence of dark matter. [The Astrophysical Journal Letters](#), 648(2):L109 (2006).
- [44] R. Massey *et al.* The behaviour of dark matter associated with four bright cluster galaxies in the 10 kpc core of Abell 3827. [Monthly Notices of the Royal Astronomical Society](#), 449(4):3393-3406 (2015).
- [45] T. A. Porter *et al.* Dark Matter Searches with Astroparticle Data. [Annu. Rev. Astro. Astrophys.](#), 49(1):155-194 (2011).
- [46] G. Bertone and D. Merritt. Dark Matter Dynamics and Indirect Detection. [Mod. Phys. Lett. A](#), 20(14):10211036 (2005).

- [47] A. Coogan and S. Profumo. Origin of the tentative AMS antihelium events. [Phys. Rev. D](#) 96, 083020 (2017).
- [48] M. Korsmeier, F. Donato and N. Fornengo. Prospects to verify a possible dark matter hint in cosmic antiprotons with antideuterons and antihelium. [Phys. Rev. D](#) 97, 103011 (2018)
- [49] Y.-C. Ding *et al.* Prospects of detecting dark matter through cosmic-ray antihelium with the antiproton constraints. [Journal of Cosmology and Astroparticle Physics](#) 1906 (2019) 004.
- [50] M. W. Winkler and T. Linden. Dark Matter Annihilation Can Produce a Detectable Antihelium Flux through  $\bar{\Lambda}_b$  Decays. [Phys. Rev. Lett.](#) 126, 101101 (2021)
- [51] A. Shukla *et al.* Large-scale simulations of antihelium production in cosmic-ray interactions. [Phys. Rev. D](#) 102, 063004 (2020).
- [52] J. Alcaraz *et al.* Search for Antihelium in Cosmic Rays. [Phys. Lett. B](#), 461:387-396 (1999).
- [53] J. Alcaraz *et al.* Protons in near Earth orbit. [Phys. Lett. B](#), 472:215-226 (2000).
- [54] J. Alcaraz *et al.* Cosmic Protons. [Phys. Lett. B](#), 490:27-36 (2000).
- [55] J. Alcaraz *et al.* Helium in near Earth orbit. [Phys. Lett. B](#), 494:193-202 (2000).
- [56] S. Ahlen *et al.* An antimatter spectrometer in space. [Nucl. Inst. Meth. A](#), 350:387-396 (1994).
- [57] T. Kirn. The AMS-02 transition radiation detector. [Nucl. Inst. Meth. A](#) 581, 156-159 (2007).

- [58] V. Bindi *et al.* The AMS-02 Time of Flight System. Final Design. [Tech. Rep. hep-ex/0305074](#), Bologna, 2003.
- [59] V. Bindi *et al.* The time of flight detector of the AMS-02 experiment on the international space station. [Nucl. Inst. Meth. A](#) 718, 478-480 (2013).
- [60] V. Bindi *et al.* The scintillator detector for the fast trigger and time-of-flight (TOF) measurement of the space experiment AMS-02. [Nucl. Inst. Meth. A](#), 2010. 623(3):968-981
- [61] K. Lbelsmeyer. *et al.* Upgrade of the Alpha Magnetic Spectrometer (AMS-02) for long term operation on the International Space Station (ISS). [Nucl. Inst. Meth. A](#) 654, 639-648 (2011).
- [62] S. Haino. Performance of the AMS-02 silicon tracker in the ISS mission. [Nucl. Inst. Meth. A](#) 699, 221-224 (2013).
- [63] J. Alcaraz *et al.* The alpha magnetic spectrometer silicon tracker : Performance results with protons and helium nuclei. [Nucl. Inst. Meth. A](#) 593, 376–398 (2008).
- [64] P. von Doetinchem *et al.* The AMS-02 Anticoincidence Counter. [Nuclear Physics B - Proceedings Supplements](#) 197, 15-18 (2009).
- [65] R. Pereira The AMS-02 RICH detector: Performance during ground-based data taking at CERN. [Nucl. Inst. Meth. A](#) 639, 37-41 (2011).
- [66] M. Vecchi *et al.* The electromagnetic calorimeter of the AMS-02 experiment. In SF2A-2012: Proceedings of the Annual meeting of the French Society of Astronomy and Astrophysics (eds. Boissier, S. *et al.*), 621-625 (2012).
- [67] T. G. Nelson. *SEARCH FOR COSMIC-RAY ANTIDEUTERONS WITH THE AMS-02 EXPERIMENT ON THE INTERNATIONAL SPACE STATION* (2019).

- [68] M. W. Winkler, P. D. L. T. Luque, and T. Linden. Cosmic ray antihelium from a strongly coupled dark sector. [arXiv:2211.00025](https://arxiv.org/abs/2211.00025) [hep-ph] (2022).
- [69] G. J. Feldman and R. D. Cousins. Unified approach to the classical statistical analysis of small signals. [Phys. Rev. D.](https://doi.org/10.1103/PhysRevD.57.3873) 57, 3873-3889 (1998).
- [70] K. Albertsson *et al.* "TMVA 4 Toolkit for Multivariate Data Analysis with ROOT". (2020), [Online].
- [71] D. Smart and M. Shea. A review of geomagnetic cutoff rigidities for earth-orbiting spacecraft. *Advances In Space Research* (2004).
- [72] L. Desorgher. "PLANETOCOSMICS Software User Manual". (2005), [Online].
- [73] L. Hennig. *Extension of the PLANETOCOSMICS framework for the calculation of geomagnetic cutoff histograms* (2022).
- [74] L. Desorgher, E. Fluckiger, and M. Gurtner. *The Planetocosmics Geant4 application*, 36th COSPAR Scientific Assembly, vol. 36 (2006).
- [75] N. A. Tsyganenko and M. I. Sitnov. Modeling the dynamics of the inner magnetosphere during strong geomagnetic storms. [Journal of Geophysical Research: Space Physics](https://doi.org/10.1029/2004JA010500), vol. 110, no. A3 (2005).
- [76] P. v. Doetinchem and B. Yamashiro, "Geomagnetic Cutoff Calculations for the Interpretation of Low-rigidity Cosmic-ray Antiparticle Measurements," unpublished draft, (2017).
- [77] N. A. Tsyganenko. *Modeling the Earth's Magnetosphere Using Spacecraft Magnetometer Data*, (2021).

- [78] D. J. Cooke *et al.* On cosmic-ray cut-off terminology, [Il Nuovo Cimento C](#), vol. 14, no. 3, pp. 213–234 (1991).
- [79] The polar aurora. By Carl Störmer. Oxford University Press, 1955. Pp. xvii, 403; 216 Figs., 27 Tables. 55s. [Quarterly Journal of the Royal Meteorological Society](#) 82, 115-115 (1956).